EUROPEAN ORGANIZATION FOR NUCLEAR RESEARCH

CERN-EP/88-148
25 October 1988

CHARM PHOTOPRODUCTION RESULTS FROM NA14′

The NA14′ Collaboration

M.P. Alvarez[1], R. Barate[2], D. Bloch[3], P. Bonamy[4], P. Borgeaud[4], M. Burchell[5], H. Burmeister[2], J.M. Brunet[6], F. Calvino[1a], M. Cattaneo[5], J.M. Crespo[1], B. D'Almagne[7], M. David[4], L. DiCiaccio[2b], J. Dixon[5], P. Druet[7], A. Duane[5], J.P. Engel[3], T.A. Filippas[8], E. Fokitis[8], R.W. Forty[5], P. Foucault[3], E.N. Gazis[8], J.P. Gerber[3], Y. Giomataris[2], T. Hofmokl[9], E.C. Katsoufis[8], M. Koratzinos[7], C. Krafft[7], B. Lefièvre[6], Y. Lemoigne[4], A. Lopez[2c], J.G. McEwen[10], C. Magneville[4], A. Maltezos[8], Th. Papadopoulou[8], B. Pattison[2], D. Poutot[6], M. Primout[4], H. Rahmani[8], P. Roudeau[7], C. Seez[5], J. Six[7], R. Strub[3], D. Treille[2], P. Triscos[6], G. Tristram[6], G. Villet[4], A. Volte[6], M. Wayne[7], D.M. Websdale[5], G. Wormser[7] and Y. Zolnierowski[2]

ABSTRACT

High statistics samples of reconstructed charmed particles have been obtained by the NA14′ experiment. Signals are presented in a variety of decay channels, and are used for the measurement of lifetimes and the study of production mechanisms.

Contribution to the
24th Int. Conf. on High-Energy Physics,
Munich, 4–10 August 1988

1 Universidad Autónoma, Barcelona, Spain.
2 CERN, Geneva, Switzerland.
3 CRN, Strasburg, France.
4 CEN, Saclay, France.
5 Imperial College, London, England.
6 Collège de France, Paris, France.
7 LAL, Orsay, France.
8 National Technical University, Athens, Greece.
9 University of Warsaw, Warsaw, Poland.
10 University of Southampton, Southampton, England.
a Univ. Politecnica de Catalunya, ETSEIB-DEN, Barcelona, Spain.
b Univ. di Roma-2, La Sapienza, Rome, Italy.
c On leave from Fac. C. Fisicas, Univ. Complutense de Madrid, Madrid, Spain.

1. Introduction

Photoproduction is of interest as it lies at the borderline between the electromagnetic and hadronic interactions. As the electromagnetic interaction is well understood, the study of charm photoproduction mechanisms provides information about the hadronic interaction, and allows QCD to be tested. The measurements of the cross-section and of the inclusive x_F distributions of charmed particles are sensitive to the gluon structure function of the target nucleon, and a study of the relative production rates of the different charmed particles provides information about the hadronisation of the charm quarks.

The gross features of the weak decay of charmed particles are understood in terms of the β-decay of the charm quark. This simple spectator model picture is, however, complicated by QCD corrections, non-spectator contributions and final-state interactions, and further results on the lifetimes and branching fractions of charmed particles are required to distinguish these effects.

A high statistics sample of charmed particles is required for such studies. The charm content of a given sample of hadronic events is greater for photoproduction than for hadroproduction, since (unlike hadrons) photons couple directly to the quarks, leading to a higher effective center-of-mass energy in the parton subprocess, available for the creation of heavy quarks. A high-resolution vertex detector is essential for the clean extraction of the charm signals.

NA14′ is a photoproduction experiment at CERN, utilising a silicon vertex detector. In this paper, preliminary results from the experiment are presented. The paper is organized as follows: in Section 2, the apparatus and data taking of the experiment are described. The charm signals that have been obtained are used in Section 3 to study charm spectroscopy, and in Section 4 to measure the lifetimes of charmed particles. Production details are considered in Section 5. Finally the conclusions are presented, and the hadronisation scheme that has been developed is discussed in an appendix.

2. The NA14′ Experiment

The NA14′ spectrometer was originally designed to study the photoproduction of photons and hadrons at high transverse momenta [1], and is characterized by a large angular acceptance for such particles. A schematic layout of the apparatus is shown in Fig. 1. For the study of charm, the chief modification to the apparatus of the previous experiment was the addition of a high-resolution silicon vertex detector. A description of this detector and some other details relevant to the current analysis are given below.

Charged particles are deflected by two magnets having a total integrated $B \cdot \ell$ of 4 Tm, and are measured by 73 MWPC planes, leading to a typical mass resolution for a D-meson of $\sigma_M \simeq 13$ MeV. Kaons are identified between 6·3 and 20·5 GeV/c by an air-filled gas Cerenkov counter C1. A second Cerenkov counter C2 filled with Freon is situated

in the high magnetic field of the second magnet. It has a pion threshold at 3·5 GeV/c and is used to distinguish protons from kaons above 10 GeV/c. Three electromagnetic calorimeters—two of lead-glass and one of lead/scintillator construction, that cover the geometrical acceptance of the apparatus—are used to reconstruct neutral particles.

To reduce the combinatorial background in mass distributions under the charmed particle signals, use of the information from the vertex detector is crucial. This detector comprises a segmented silicon target, with analogue read-out [2], and a set of ten planes of 50 μm pitch microstrips, with an active area of $5 \times 5\,\mathrm{cm}^2$ and digital read-out [3]. See Fig. 2.

The silicon active target is segmented along the beam direction in 500 μm steps (300 μm of silicon, 200 μm of air). Each plane of silicon is subdivided into 2·1 mm slabs in a plane transverse to the beam. The analogue signals give a measurement of the ionization deposited around the vertex position.

The telescope of microstrip planes permits the reconstruction of charged particle tracks with a transverse accuracy of $\sim 17\,\mu$m at the vertex. The planes are arranged in 5 pairs, with the members of each pair oriented so that their strips are orthogonal. The first four pairs are arranged horizontally/vertically, whilst the fifth pair is rotated by $\sim 33°$ to provide matching of projection tracks in space. A minimum ionizing particle gives a signal with a mean value (1 *minI*) of ~ 14 times the noise fluctuation. The read-out discriminator threshold is set to 35 % *minI* to ensure that the signal of a track that crosses two strips is still registered. The number of spurious hits generated over the whole detector is about 6 in a 50 ns gate, and the charge sharing is low, as 90 % of clusters are single hits. Due to financial constraints, each data acquisition channel was used to read two strips—the connection of the strip pairs was arranged so that aligned hits from a charged track give dispersed hits for the paired channels. The per-plane efficiency of the microstrip detector was measured under normal operating conditions to be $\sim 97\,\%$, independent of the track angle (up to 150 mrad).

The importance of the vertex detector in the isolation of charmed particle signals is illustrated in Fig. 3 for the decay* $D^+ \to K^-\pi^+\pi^+$, from a sub-sample of the data. This good background rejection permits the reconstruction of charmed particles with a kaon momentum above the 20 GeV/c threshold of C1; thus the number of reconstructed $D^0 \to K^-\pi^+$ decays is doubled with only $\sim 5\,\%$ of ambiguous entries ($K\pi \leftrightarrow \pi K$).

Trigger conditions and data acquisition

The trigger of the experiment is designed to select hadronic interactions of the incident photon beam. Most of the photon interactions in the silicon target are electromagnetic, leading to the production of e^+e^- pairs that are created collinear to the beam. When they pass through the magnetic fields of the spectrometer, the pairs are swept into a

* Charge conjugate states are implicitly included throughout this paper, except for the discussion of particle-antiparticle asymmetries.

horizontal band. The trigger makes use of this feature, and requires at least one charged particle above and below the horizontal region, determined using scintillator hodoscopes as illustrated schematically in Fig. 4. Further rejection of pairs is achieved with a target condition that there should be at least 2·5 *minI* of charge deposited. Upstream of the target, scintillator counters are used to veto muons that form a halo to the experimental beam, and to ensure that the incident photon has not converted before reaching the target.

The trigger efficiency is $\sim 30\,\%$ for non-charmed hadronic interactions, rising with energy. For charm events, the efficiency is ~ 2 times higher because of the greater charged track multiplicity, and because the particles are emitted with a higher mean transverse momentum. The hadronicity of registered events is $\sim 85\,\%$.

The experimental photon beam is produced by the bremsstrahlung of electrons, which are generated indirectly from the protons of the CERN SPS. Every 12 s a burst of 8×10^7 electrons is incident, over a period of 2 s, on a $10\,\%$ X_0 lead radiator. The resulting photon beam has high luminosity ($\sim 10^7$/burst, $E_\gamma > 50$ GeV), and negligible hadron contamination. About 60 events are registered on tape per burst. Over the period 1985–1986 a total of ~ 17 million events were recorded.

Data processing

The events are first passed through a fast algorithm that reconstructs charged tracks using the MWPC information, and identifies kaons. It is then necessary to select events of interest to particular lines of analysis using fast filter algorithms, to give a manageable sample for passing through the complete off-line reconstruction programs.

To search for D_s^+ and Λ_c decays, events with two kaons or one kaon and one proton were selected, signed in Cerenkov C1.

For the D^0 and D^+-meson analysis, the vertex detector information was used to enrich the charm content of the data. This was achieved by matching the tracks seen in the chambers with the corresponding hits in the microstrips. The active target was used to define the primary vertex position along the beam direction, and matched tracks were extrapolated to this position to define the primary vertex coordinates in the transverse plane. These coordinates are then used, in a second pass, to associate unmatched tracks with microstrip information. The charm content of the data could then be enhanced by rejecting events for which the tracks were compatible with a single vertex. In this manner $\sim 18\,\%$ of the recorded events were kept, to be passed through the full reconstruction. The efficiency of this 'microstrip' filter for charm interactions was measured as $\sim 50\,\%$.

Towards the end of 1987 ~ 5 million events were processed directly through the full reconstruction, using the emulator farm facility at CERN—utilising up to ten 3081/E emulators [4]. This data-set is important for the investigation of filter efficiencies and biases.

Charm analysis

The combination of tracks for a given charmed particle decay is chosen using the Cerenkov information. The decay tracks are required to be reconstructed in the microstrip detector, and are used to find the decay vertex. For $K\pi$ events the accuracy along the beam direction is about 500 μm (see Fig. 5). The trajectory of the candidate charmed particle is then reconstructed, and used along with the remaining tracks in the event to search for the production vertex. If the chi-square of the vertex fit is unacceptable then the least well associated track—which might come from the second charm decay in the event, or be badly reconstructed—is rejected, and the process iterated.

The charm signals are then extracted by imposing a cut on the separation of the production and decay vertices, applied either to their separation distance along the beam direction, Δx, or to this distance divided by its error σ_x (determined from the errors on the vertices), $N_\sigma = \frac{\Delta x}{\sigma_x}$.

The charm signals reconstructed using this procedure are shown in the following section. These signals have been used to search for events in which the second charm decay can be reconstructed, for the study of associated production. Such an event is displayed in Fig. 6 (a), where the two projections along the beam direction are shown. The two decays $D^+ \to K^-\pi^+\pi^+$ and $D^- \to K^+\pi^-\pi^-$ are clearly seen. The ionization deposited in the active target is also displayed, and agrees with the microstrip information, with a large pulse height at the production vertex (from nuclear recoil) and a multiplicity step at the secondary vertex that lies within the target.

The active target information is also useful for the rejection of secondary interactions, which can mimic charm decays. An example is given in Fig. 6 (b), where the ionisation deposited in each target slab is displayed as a number of *minI* equivalent. The nuclear activity at the reconstructed secondary vertex indicates that this is a secondary interaction.

3. Spectroscopy of Charmed Particles

D decays

High statistics samples of reconstructed D^0 and D^+ decays have been obtained. The D^0 and D^+ signals used for our inclusive analysis are shown in Fig. 7. These include ~ 650 $D^0 \to K^-\pi^+$ decays, ~ 370 $D^0 \to K^-\pi^+\pi^+\pi^-$ decays and ~ 450 $D^+ \to K^-\pi^+\pi^+$ decays. Also shown is a signal for D^0 coming from the decay $D^{*+} \to D^0\pi^+$, extracted with the requirement that the mass difference $(m_{D^*} - m_{D^0})$ lies in the range 143–149 MeV/c^2.

A signal has been obtained in the channel $D^0 \to K^-\pi^+\pi^0$, shown in Fig. 8. The $D^0 \to K^-K^+$ decay mode is shown in Fig. 9. Unambiguous kaon identification in the Cerenkov counter cannot be imposed for the analysis of this channel without a severe loss of acceptance, so the kaon identification criteria are relaxed to include particles with momentum greater than the kaon threshold (20·5 GeV/c). As a result, enhancements are

seen on both the high and low mass sides of the D^0 peak, corresponding respectively to the decays $D^0 \to K^-\pi^+$ and $D^0 \to K^-\rho^+ \to K^-\pi^+(\pi^0)$, in which the pion has been considered as a kaon. We measure :

$$\frac{Br(D^0 \to K^+K^-)}{Br(D^0 \to K^-\pi^+)} = 0{\cdot}16 \pm 0{\cdot}03.$$

We have looked for the decay $D^0 \to \phi\pi^+\pi^-$ (Fig. 10). The two kaons are identified by the Cerenkov counter without a substantial loss of acceptance for this channel. We measure :

$$\frac{Br(D^0 \to \phi\pi^+\pi^-)}{Br(D^0 \to K^-\pi^+)} = 0{\cdot}14 \pm 0{\cdot}06 \pm 0{\cdot}02,$$

and using the branching ratio for $D^0 \to K^-\pi^+$ measured by the Mark III collaboration $(4{\cdot}2 \pm 0{\cdot}4\,\%)$, we obtain:

$$Br(D^0 \to \phi\pi^+\pi^-) = 0{\cdot}59 \pm 0{\cdot}27 \pm 0{\cdot}13\,\%.$$

D_s decays

D_s^+-mesons have been studied in final states involving two charged kaons. In Fig. 11 the $\phi\pi^+$ channel is shown, with data taken from both the two-kaon and the microstrip filters. A clear signal is seen for the decay $D_s^+ \to \phi\pi^+$, and also for the Cabibbo suppressed D^+ decay into the same final state. The $K^{*0}K^+$ decay mode shown in Fig. 12 exhibits a signal at the D_s^+ mass, but there is no evidence for a signal at the D^+ mass.

From these measurements we obtain [5]:

$$\frac{D^+ \to K^{*0}K^+}{D^+ \to \phi\pi^+} \leq 1{\cdot}0 \quad (\text{at } 90\,\%\text{ CL}),$$

$$\frac{D_s^+ \to K^{*0}K^+}{D_s^+ \to \phi\pi^+} = 0{\cdot}93 \pm 0{\cdot}37.$$

This shows, as already observed for the decays $D^0 \to K^-\pi^+$ and $D^0 \to \overline{K}^0\pi^0$, that the so-called 'colour suppression' mechanism does not operate—it would lead to an enhancement of the decay to K^*K^+ for the D^+ and of the decay to $\phi\pi^+$ for the D_s^+.

We have searched for signals in the $\phi\pi^+\pi^0$ final state (Fig. 13). The efficiency of π^0 reconstruction has been obtained from a Monte Carlo simulation, and has been verified using the D^0 decay into $K^-\pi^+\pi^0$. We find no evidence for a D_s^+ signal, and obtain the limit:

$$\frac{D_s^+ \to \phi\pi^+\pi^0}{D_s^+ \to \phi\pi^+} < 3{\cdot}5 \quad (\text{at } 90\,\%\text{ CL}).$$

This result contradicts expectations from the model of Ref. [6] which predicts a value of 6·3 for the ratio $D_s^+ \to \phi\rho^+/D_s^+ \to \phi\pi^+$. In the D^+ mass region 7 events are seen, and the background is estimated as 2 events, leading to:

$$Br(D^+ \to \phi\pi^+\pi^0) = 5 \pm 3 \pm 1\,\%.$$

This value is large for a Cabibbo suppressed decay, although the measurement is clearly of limited accuracy.

Λ_c decays

The Λ_c-baryon has been identified in the $pK^-\pi^+$ final state (Fig. 14). Protons are unambiguously identified using the information from both Cerenkov counters. A signal of ~ 26 events is observed, over a similar background. The properties of this signal are currently under investigation, and measurements of its lifetime and other characteristics will follow shortly.

D^{**} decays

The higher angular excitations of the D-mesons have recently been observed by the CLEO, ARGUS and E691 collaborations. If the value of $\sigma \cdot Br$ for the decay$D^{**0} \to D^{*+}\pi^-$ were the same as in e^+e^- annihilations, we would expect to see ~ 20 events. The mass difference $(m_{D^*\pi} - m_{D^*})$ is plotted in Fig. 15 (a), and shows an enhancement at $\sim 0{\cdot}4\,\mathrm{GeV}/c^2$ of about 24 events. No enhancement is seen in the distributions found using either events from the wings of the D^* mass plot (b) or wrong sign combinations (c).

The $D^0\pi^+$ decay mode is shown in Fig. 16 (a). A clear peak is, of course, seen for the D^{*+}, and there is in addition an enhancement that may indicate the D^{**+}. Similarly for the D^0K^+ mode shown in Fig. 16 (b) there is an enhancement at $\sim 2520\,\mathrm{MeV}/c^2$, that may indicate a $D_s^{**+} \to D^0K^+$ decay. These indications are all, however, of only $\sim 3\,\sigma$ significance.

4. Lifetime Measurement

A maximum likelihood method is used to measure the charmed particle lifetimes. For each event, i, the vertex separation cut—used to extract the charm signals—defines the minimum accessible proper time t^i_{min}. The maximum proper time, t^i_{max}, is determined by the distance between the primary vertex and the first microstrip plane.

The probability distribution is taken as:

$$P(t) = (1 - \epsilon_0)P_S(t) + \epsilon_0 P_B(t),$$

normalized to unity between t^i_{min} and t^i_{max}. Here ϵ_0 is the ratio of the number of events coming from the background to the total number of events at $t = 0$. This is not the same as the background fraction ϵ that is measured from the mass distribution of the selected events, and an iterative technique is used to determine a value for ϵ_0 that reproduces the measured ϵ.

The probability distributions for the signal $P_S(t)$ and for the background $P_B(t)$ are of the form $P(t) = A(t)f(t)$, where $f(t)$ has an exponential dependence convoluted with

a Gaussian distribution to take account of the detector resolution. This distribution is normalized to unity for t varying between $-\infty$ and $+\infty$. $A(t)$ corrects for variation of the acceptance with the measured proper time, determined using both a Monte Carlo simulation and reconstructed K_s^0 decays.

D_s^+ lifetime

Events are selected in the $\phi\pi^+$ decay mode, using data from the two-kaon filter. The D_s^+ signal is defined from the mass distribution, taking events that have mass within $25\,\mathrm{MeV}/c^2$ of the D_s^+ mass.

The acceptance is determined using Monte Carlo data. The proper lifetimes measured for events that pass the analysis chain are compared with the exponential distribution with which the events were generated. The ratio of the measured distribution to the input distribution (normalized to contain the same number of events) is shown Fig. 17. Two features are evident in the acceptance correction:

- a small depletion at short times. This is mainly caused by an offset track requirement of the analysis;
- a depletion at long times (greater than about 3 ps). This is a result of the fiducial cut imposed at the microstrip detector. Its effect is insignificant for the D_s^+ lifetime.

The effective lifetime of the background, τ_B, was measured using events taken from the wings of the mass plot (excluding the D_s^+ and D^+ signal regions). See Fig. 18. We find $\tau_B = 0{\cdot}18 \pm 0{\cdot}03$ ps.

The measured lifetime of the D_s^+ signal, with background and acceptance corrections, is stable for a selection of vertex separation cuts in Δx and N_σ. Taking the measurement that gives the least fractional errors (at $\Delta x > 1{\cdot}5\,\mathrm{mm}$) we obtain $\tau_{D_s} = 0{\cdot}33\ ^{+0{\cdot}12}_{-0{\cdot}08}$ ps. See Fig. 19. Without the acceptance and background corrections this value is reduced by $\sim 6\,\%$, demonstrating that the corrections are small.

A potential source of systematic error for this measurement is reflections from other channels—i.e. the contamination of the signal with particles of a different type, which have been reconstructed with the D_s^+ mass due to misidentification of their decay products. The two most likely candidates are $\Lambda_c^+ \to pK^-\pi^+$ and $D^+ \to K^-\pi^+\pi^+$. The masses of the events used for the lifetime measurement were recalculated assuming each of the above reflection hypotheses in turn. Those events that were then found to lie within the Λ_c^+ or D^+ mass ranges respectively were excluded and the lifetime recalculated, giving $\tau_{D_s} = 0{\cdot}33\ ^{+0{\cdot}14}_{-0{\cdot}09}$ ps (Λ_c^+ reflections excluded), and $\tau_{D_s} = 0{\cdot}32\ ^{+0{\cdot}15}_{-0{\cdot}10}$ ps (D^+ reflections excluded). The effect of the candidate reflections on the measured lifetime is therefore insignificant.

Statistical uncertainty in the acceptance correction gives a contribution to the systematic error. This contribution was minimised by using a large Monte Carlo sample of D_s^+ decays, generated with a nominal lifetime of 0·4 ps. The reconstructed lifetime was $\tau_{D_s}(MC) = 0{\cdot}430\ ^{+0{\cdot}037}_{-0{\cdot}033}$ ps, and the statistical accuracy of this measurement leads to a contribution to the systematic error of $\sigma_{syst}(\text{acceptance}) = {}^{+0{\cdot}028}_{-0{\cdot}025}$ ps.

A further source of systematic error is the uncertainty on the background correction. The background fraction and effective lifetime both have associated errors; to determine the resulting systematic error, the D_s^+ lifetime was calculated using each of the values adjusted by $\pm 1\,\sigma$ error, giving σ_{sys}(background fraction) = $^{+0.010}_{-0.009}$ ps, and σ_{sys}(background lifetime) = $^{+0.004}_{-0.005}$ ps.

The various contribution to the systematic error are assumed to be independent, and are added in quadrature to give:

$$\tau_{D_s} = 0{\cdot}33\ ^{+0.12}_{-0.08} \pm 0{\cdot}03 \text{ ps}.$$

D^0 lifetime

The D^0 signal used for the lifetime measurement is taken from the $K^-\pi^+$ and $K^-\pi^+\pi^+\pi^-$ decay channels extracted from filtered data.

The acceptance correction has been determined using a Monte Carlo generation, as discussed above for the D_s^+ lifetime measurement. A sample of reconstructed K_s^0 decays has also been used, and gives similar results, as shown in Fig. 20. This correction changes the measured D^0 lifetime by $\sim 3\,\%$. The time evolution of background events does not have a simple exponential behaviour at low N_σ cut, as shown in Fig. 21 (a), so two exponential slopes have been used.

The lifetime measured for the signal is stable for various selection criteria and we obtain (Fig. 21 (b)):

$$\tau_{D^0 \to K\pi} = 0{\cdot}404 \pm 0{\cdot}029 \pm 0{\cdot}040 \text{ ps} \qquad (N_\sigma > 4)$$

$$\tau_{D^0 \to K3\pi} = 0{\cdot}414 \pm 0{\cdot}035 \pm 0{\cdot}040 \text{ ps} \qquad (N_\sigma > 8)$$

If we combine these two measurements we get :

$$\tau_{D^0} = 0{\cdot}409 \pm 0{\cdot}022 \pm 0{\cdot}040 \text{ ps}.$$

D^+ lifetime

Events are lost at large decay lengths in the filtered data, as seen in Fig. 20. This has marginal influence on the measurement of the D^0 lifetime, as shown above, but affects the D^+ to a greater extent due to its longer lifetime. For the D^+ we have therefore used the data processed directly through the emulator farm, which do not suffer from this problem.

The measured D^+ lifetime is :

$$\tau_{D^+} = 0{\cdot}95 \pm 0{\cdot}06 \pm 0{\cdot}09 \text{ ps} \qquad (N_\sigma > 6),$$

and the corresponding distributions are shown in Fig. 22.

Note: the values quoted for the D^0 and D^+ lifetimes are still preliminary, and the control of systematic errors is under study.

5. Inclusive Charm Photoproduction

The suitability of incident photons for QCD tests

In the previous NA14 experiment [1] the photoproduction of hadrons was measured at moderate and high transverse momenta. The agreement with perturbative QCD was impressive, in contrast to the results of hadroproduction in the same p_T range. In particular the QCD component is large, of similar amplitude to the vector meson dominance model (VDM) component when $p_T > 2\,\mathrm{GeV}/c$, and the agreement with theory is good down to $p_T \sim 1{\cdot}6\,\mathrm{GeV}/c$. The reasons for such a behaviour of incident photons are studied in detail in Ref. [7]. In these processes the interaction of the photon with matter has three components—depending on the scale of its coupling to matter, the photon:

- behaves like a hadron for $Q^2 \sim \Lambda^2$, giving the so-called 'VDM component' of the interaction;
- behaves like a parton for $Q^2 \sim p_T^2$, corresponding to a point-like coupling to the other partons;
- has an anomalous component which can be obtained from QCD.

For charm photoproduction an even simpler situation is therefore expected, since the large mass of the charm quark permits the 'VDM component' to be computed in perturbative QCD: $p_T \sim m_c \gg \Lambda$. Furthermore the contribution of the anomalous component is also expected to be small [8]. At first order in QCD a single diagram remains—γg-fusion—and if the energy dependence of the cross-section is measured, information will be gained about the gluon structure function $G(x)$ of the nucleon. The p_T dependence of charm photoproduction gives access to m_c.

Measurement of the charm photoproduction cross-section *

In the experimental beam line, a tagging system measures the energy radiated by the incoming electron when it crosses the lead radiator. This system is also used in the trigger logic to ensure a minimum radiated energy of $\sim 50\,\mathrm{GeV}$. A simulation program is used to correct for the difference between the measured tagging energy and the real photon energy due to multiple bremsstrahlung. The program uses the measured incident electron energy spectrum and reproduces the observed tagging energy distribution.

The charm photoproduction cross-section is obtained from the following relation:

$$N_D^S = N_H \times \frac{\epsilon_D^T}{\epsilon_H^T} \times P_D \times \frac{\sigma_C}{\sigma_H} \times \epsilon_D^S \times Br_D$$

- N_D^S = number of selected charmed particles using a given set of cuts;
- N_H = number of hadronic events which fulfil the trigger conditions;
- $\epsilon_D^T, \epsilon_H^T$ = triggering efficiencies to charm and hadronic interactions;

* This measurement is obtained using a half of the available statistics.

- ϵ_D^S = efficiency for the cuts used to select the considered charmed particles in addition to the trigger requirements. These cuts include the kaon signature in the Cerenkov counter, the measurement of charged tracks in the microstrip telescope, the reconstruction of secondary and primary vertices and the cut on the vertex separation.
- $\sigma_H = \gamma N$ hadronic cross-section;
- σ_C = charm photoproduction cross-section;
- P_D = mean number of charmed particles of a given flavour produced in one charm event ($\sum_D P_D = 2$);
- Br_D = branching fraction of the considered charmed particle into the observed final state.

For the measurement of ϵ_H^T, interactions produced by a 90 GeV energy π^- beam have been isolated by scanning a sample of events registered without any triggering condition (apart from the requirement of the presence of a particle in the beam). Using the known $\pi^- N$ cross-section, the trigger efficiency has been deduced from the number of events satisfying the trigger conditions of the normal data-taking period:

$$\epsilon_H^T\ (90\,\mathrm{GeV}) = 29 \pm 6\,\%$$

(The accuracy of this measurement is dominated by the statistics of scanned events and will be improved). To account for the energy variation of the trigger efficiency a Monte Carlo generator has been developed which simulates γN hadronic interactions in the target. It incorporates the geometry and efficiency of the various apparatus components, and the measured efficiency at 90 GeV is well reproduced by this simulation.

Charm events have also been generated, using γg-fusion, and are entered into the simulation program mentioned above. The scheme for the hadronisation of the event final states is described in the Appendix. These events are used to determine the trigger efficiency for charm events, ϵ_D^T, which is typically $2 \times \epsilon_H^T$. The simulation is also used to determine P_D.

We measure :

$$\sigma_C = 450 \pm 50\ ^{+100}_{-120}\ \mathrm{nb} \qquad \text{at } E_\gamma \sim 100\mathrm{GeV}.$$

The energy dependence of the charm photoproduction cross-section is shown in Fig. 23. Also shown are measurements published by other photoproduction experiments, and those obtained by muoproduction experiments extrapolated to $Q^2 = 0$. A preliminary result from E691 [9] is also indicated. All of these measurements are in reasonable agreement with the first order QCD γg-fusion model with the following parameters:

$$xG(x) = 3(1-x)^5,\ Q^2 = m_c^2,\ \Lambda = 200\,\mathrm{MeV},\ m_c = 1{\cdot}5\,\mathrm{GeV}/c^2.$$

A second order computation is now available [8b].

x_F and p_T distributions * of charmed particles

The measured p_T and x_F^{Tag} distributions** of charmed particles are compared with those simulated according to the γg-fusion mechanism in Figs. 24 and 25 (a).

The p_T distribution of background—measured using events from the wings of the mass distributions—is well described by an e^{-6m_T} parameterisation (where m_T is the transverse mass), also indicated on Fig. 24. The p_T distribution for the signal events shows a clear excess at high p_T. The prediction from the simulation is sensitive to the charm quark mass, and a value of $m_c \sim 1{\cdot}5\,\mathrm{GeV}/c^2$ is favoured by the data.

The x_F^{Tag} distribution of the data has not been corrected for the contribution from multiple bremsstrahlung, but this effect has been included in the Monte Carlo simulation, so the comparison of data and simulation distributions is valid.

The dependance of the acceptance versus x_F is shown in Fig. 25 (b). The x_F distribution is quite insensitive to the choice of the charm quark mass. It becomes narrower (Fig. 26 (a)), as expected, if the gluon structure function is softer, and depends mainly on the choice of the charm quark fragmentation function as shown in Fig. 26 (b).

Study of hadronisation mechanisms

At the parton level, the structure of a charm photoproduction event is particularly simple since only the γg-fusion diagram is expected to contribute. The study of these events will thus provide information on the hadronisation mechanisms. Two classes of events must be considered:

- Diffractive events in which the photon produces a low mass $D\overline{D}X$ system with an exponentially falling transfer distribution. The projectile and target hadronic systems are hadronised independently. This class of events contains coherent interactions.
- Non-diffractive events in which the charm and anticharm quarks hadronise independently.

From theoretical arguments it can be shown that the fraction of diffractive events is small. For non-charmed interactions it is usually of the order of 20 %, and for charm events only a few percent is expected. A preliminary search for coherent events using the information from our active target confirms this evaluation [10].

The technique used to produce complete charm events, starting from a set of partons with momentum 4-vectors given by QCD, is described in the Appendix. Only non-diffractive events are considered. Starting from a fully symmetric situation in terms of c and $\bar{c}$ quarks, the hadronisation generates particle-antiparticle asymmetries for each type of charmed particle. At high energies a small excess of $\overline{D}^0$ (and D^-) over D^0 (D^+) is expected, whereas for D_s-mesons the reverse applies. The testing of these fine details,

---

* x_F distributions are obtained with a half of the available statistics.

** Tag indicates that, instead of the exact incident photon energy, the total energy measured by the tagging system has been used to compute x_F.

which reflect basic principles of the hadronisation scheme, requires a very large sample of D-mesons.

For NA14' the measured effects are at the limit of statistical accuracy. Calculating the asymmetry as:

$$A_D = \frac{N_D - N_{\overline{D}}}{N_D + N_{\overline{D}}},$$

we find:

$$N_D = 620 \pm 40, \quad N_{\overline{D}} = 664 \pm 40, \quad A_D = -0{\cdot}03 \pm 0{\cdot}05;$$

$$N_{D_s} = 21, \quad N_{\overline{D}_s} = 13, \quad A_{D_s} = +0{\cdot}24 \pm 0{\cdot}17.$$

The production ratio of D_s^+ and D^+-mesons also provides information concerning the hadronisation, since to produce a D_s^+-meson the charm quark must combine with a strange quark from the sea (so D_s^+ production is suppressed relative to D^+). The ratio has been measured in the $\phi\pi^+$ channel, where there are signals for both particles and the systematic errors are thus reduced. A correction is made for the lifetime behaviour of the signals in the acceptance calculation, by using a weight w for each event, given by:

$$w^i = \frac{1}{\int_{t^i_{min}}^{t^i_{max}} f(t)\, dt},$$

where $f(t)$ is the probability function from the lifetime measurements. We find:

$$\frac{\sigma \cdot Br(D_s^+ \to \phi\pi^+)}{\sigma \cdot Br(D^+ \to \phi\pi^+)} = 3{\cdot}2 \pm 1{\cdot}0\ ^{+0{\cdot}9}_{-0{\cdot}7},$$

where the systematic error is dominated by the error from the lifetime measurements. There are no convincing measurements of absolute D_s^+ branching fractions, but if a value of $Br(D_s^+ \to \phi\pi^+) \sim 4 \pm 1\,\%$ is taken, along with $Br(D^+ \to \phi\pi^+) = 0{\cdot}68 \pm 0{\cdot}07 \pm 0{\cdot}12\,\%$ (from E691), we find $\frac{\sigma(D_s^+)}{\sigma(D^+)} = 0{\cdot}54 \pm 0{\cdot}17 \pm 0{\cdot}23$. Alternatively, assuming the value for this ratio of $\sim 0{\cdot}4$ from the Monte Carlo simulation (see Appendix), we find $Br(D_s^+ \to \phi\pi^+) = 5{\cdot}4 \pm 1{\cdot}7 \pm 1{\cdot}8\,\%$.

6. Conclusions

High statistics samples of charmed particles have been obtained, and some rare decay modes of D^0 and D^+-mesons have been measured. Results on the decay of the D_s^+ to final states containing two vector mesons demonstrate that these processes are over-estimated by models [6] (supporting a similar conclusion that may be drawn from the measurement of $D^0 \to K^{*-}\rho^+$ by the Mark III collaboration).

Preliminary lifetime measurements have been presented for the D^0, D^+ and D_s^+-mesons, and are all in agreement with the corresponding world averages.

The agreement between the data on inclusive charm photoproduction and the predictions from QCD is very good which indicates that the charm quark is heavy enough to enter into the 'perturbative domain'.

A model has been developed for the final state hadronisation, and is used to predict charmed particle production rates. This permits the measurement of absolute branching ratios for the D_s^+ (and the Λ_c). The measured particle-antiparticle asymmetries support the predictions of the model.

Appendix

A generator for charm events has been developed [11], using the Dual Parton Model [12] to define the string structure of the final state and the x_F distributions of the spectator partons. The string hadronisation is performed using the Lund model.

Hadrons are produced along two strings: one 'baryonic' string stretched between the charm quark and the target spectator diquark, and one 'mesonic' string stretched between the anticharm quark and the remaining target spectator quark. See Fig. 27.

An 'intrinsic' p_T^2 of $0{\cdot}1\,(\mathrm{GeV}/c)^2$ has been attributed to the target spectator quark and diquark partons. After a gluon is removed from the nucleon target, the remaining system is transformed into a quark-diquark pair. The quark takes the fraction:

$$x_q = \frac{E_q + P_{\|q}}{E^0 + P^0}$$

where E^0 and P^0 refer to the target system.

To ensure energy-momentum balance the quark and diquark have been assigned a mass-squared which can become negative :

$$m_q^2 = \frac{M_p^2 \times x_q \times (1 - x_q) - p_T^2}{3x_q + 1},$$

$$m_Q = 2m_q,$$

so that for x_q=0, $m_q^2 = -p_T^2$; and for x_q=1, $m_Q^2 = -p_T^2$.

An additional technical detail concerns the treatment of low mass strings, in particular for the mesonic string. The program generates a continuous mass distribution which starts around $M \sim m_c$ and receives contributions below the production threshold of a physical particle. Three mass intervals are considered for the string, as shown in Fig. 28:

- region 1: in which discrete mass states are produced (D and D^* for charmed events, $\pi, \eta, K, \ldots$ for 'normal' (non-charmed) events);
- region 2: concerns only 'normal' events where low mass resonances ($\rho, \omega, K^*, \ldots$) are produced with a finite width. For these particles the string mass is assigned to the resonance mass;
- region 3: the Lund model is used to hadronise the string (in the latest version of the Lund generator the treatment of low mass systems is handled by the program).

Our approach has been not to alter the original string mass distribution, and to get the correct hadronic multiplicity for low mass systems. This is important when this type of generator is used to produce 'normal' events, since one string usually has a very low mass

distribution, peaked at threshold. This is also the case when the D.P.M. is applied to hadronic interactions at very high energies, in which a large number of low mass strings are created with partons extracted from the sea of the two colliding objects.

Another quantity which affects the multiplicity of the simulated events is the parton fragmentation function, for which results from low-p_T physics are applied, giving a $1/\sqrt{1-z}$ behaviour at high z [13]. Fig. 29 demonstrates how well the mean multiplicity distribution is reproduced for non-diffractive 'normal' events. The low-p_T inspired fragmentation functions have the consequence of decreasing the generated multiplicity relative to the 'standard' procedure. The mean charged track multiplicity for charm events—including the decay products of the charm particles—is expected to be higher than the charged multiplicity of normal events by two units.

The x_F distributions of the spectator partons are also extracted from low-p_T physics. For quarks, at small x_F, a $1/\sqrt{x_F}$ behaviour is expected, whereas for diquarks we get $x_F^{3/2}$. This implies that most of the target energy is taken by the diquark, and consequently the two strings will have very different masses as shown in Fig. 30.

Low mass strings can enhance or suppress the production of some of the different charm particle species. For low masses of the baryonic string Λ_c production is favoured relative to DN final states. This behaviour has a sharp energy dependence and has to be entered by hand into the simulation. For this purpose a minimum string mass has been defined—4 GeV/c^2—below which only Λ_c-baryons are produced, and above which a DNX system is generated. This value has been chosen to reproduce the measurement at $E_\gamma = 20$ GeV of the SHF collaboration. A continuous, instead of sharp, separation between the two final states can also be chosen, as explained in Ref. [8a].

For low masses of the 'mesonic string' the production of $\overline{D}_s$ and $\overline{\Lambda}_c$ is inhibited because of the need to produce an additional kaon or nucleon. The default values for the parameters of the Lund generator have been used for the production rates of strange particles, baryons and vector states.

Detailed predictions of the abundances of the various charmed particle species are obtained for a given incident photon energy. See Fig. 31. Results from previous photoproduction experiments WA4, WA58 and SHF are well reproduced. For instance the WA58 measurement of 11 Λ_c and no $\overline{\Lambda}_c$ is well understood.

For high energy photons the expected asymmetries between the charmed and anti-charmed particles are small, apart from for Λ_c-baryons; they have low energy, however, and are therefore not easily measured experimentally. Whilst an excess of $\overline{D}$ over D-mesons is expected, coming from the Λ_c production, for D_s-mesons the reverse is true because of the inhibition of $\overline{D}_s$.

References

[1] P.Astbury et al., *Phys. Lett.* **152B** (1985) 419.
E.Augé et al., *Phys. Lett.* **168B** (1986) 163.
R.Barate et al., *Phys. Lett.* **174B** (1986) 458.

[2] R.Barate et al., *Nucl. Instr. and Meth.* **A235** (1985) 235.

[3] G.Barber et al., *Nucl. Instr. and Meth.* **A253** (1987) 530.

[4] M.Koratzinos, NA14' internal note, NA14/88–02.

[5] C.Magneville, Thèse d'Etat (1987), C.E.N. Saclay.

[6] M.Bauer, B.Stech, M.Wirbel, *Z. Physics C., Particles and Fields* **34** (1987) 103.

[7] P.Aurenche et al., *Nucl. Phys.* **B286** (1987) 553.

[8] (a) M.Fontannaz et al., *Particles and Fields* **11** (1981) 211.
(b) R.K.Ellis and P.Nason, *Fermilab–Pub* 88/54–T (June 1988).

[9] D.J.Morrison, *Moriond conference*, 13–19$^{\text{th}}$ March 1988.

[10] M.Primout, Thèse d'Etat (1987), C.E.N. Saclay.

[11] C.Krafft, Thèse, LAL 87–28, June 1987.
P.Roudeau, *Nucl. Phys. B (Proc. Suppl.)* **1B** (1988) 33.

[12] A.Capella and J.Tran Thanh Van, *Phys. Lett.* **93B** (1980) 146.

[13] X.Artru, *Z. Physics C., Particles and Fields* **26** (1984) 83.

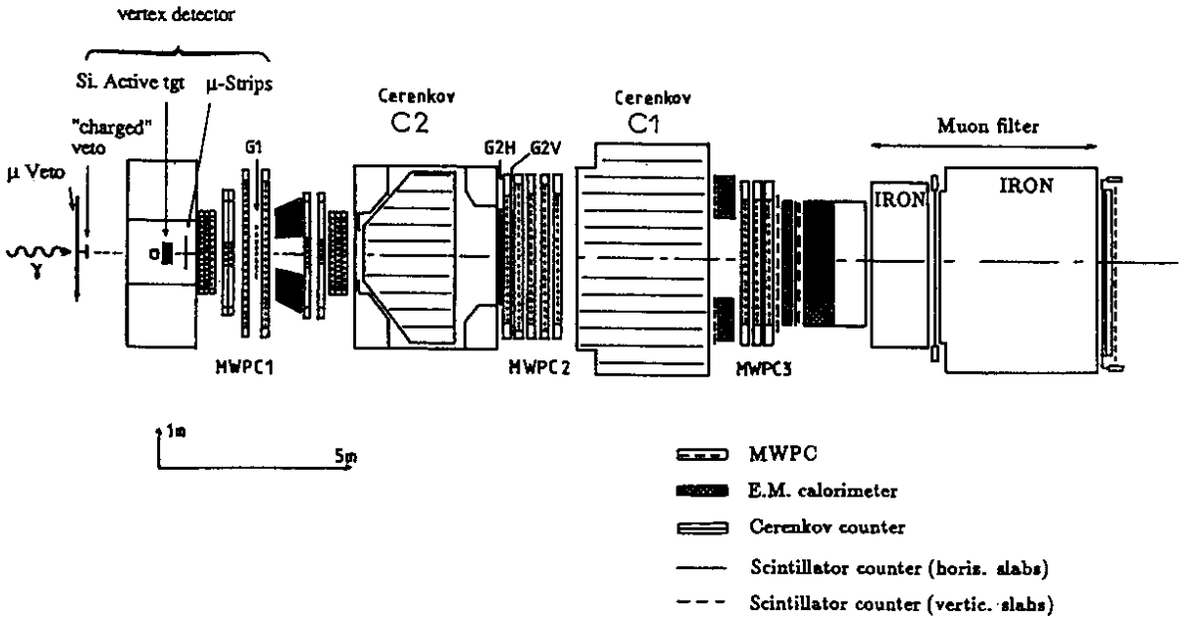

Fig. 1. The NA14′ spectrometer.

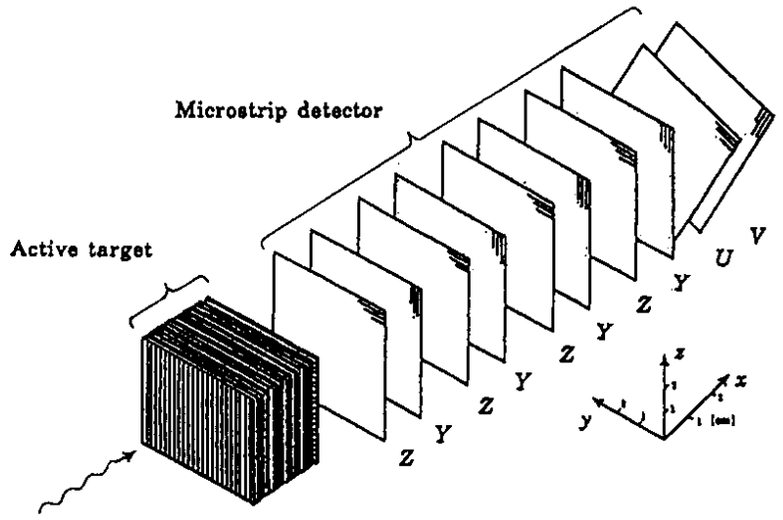

Fig. 2. The vertex detector.

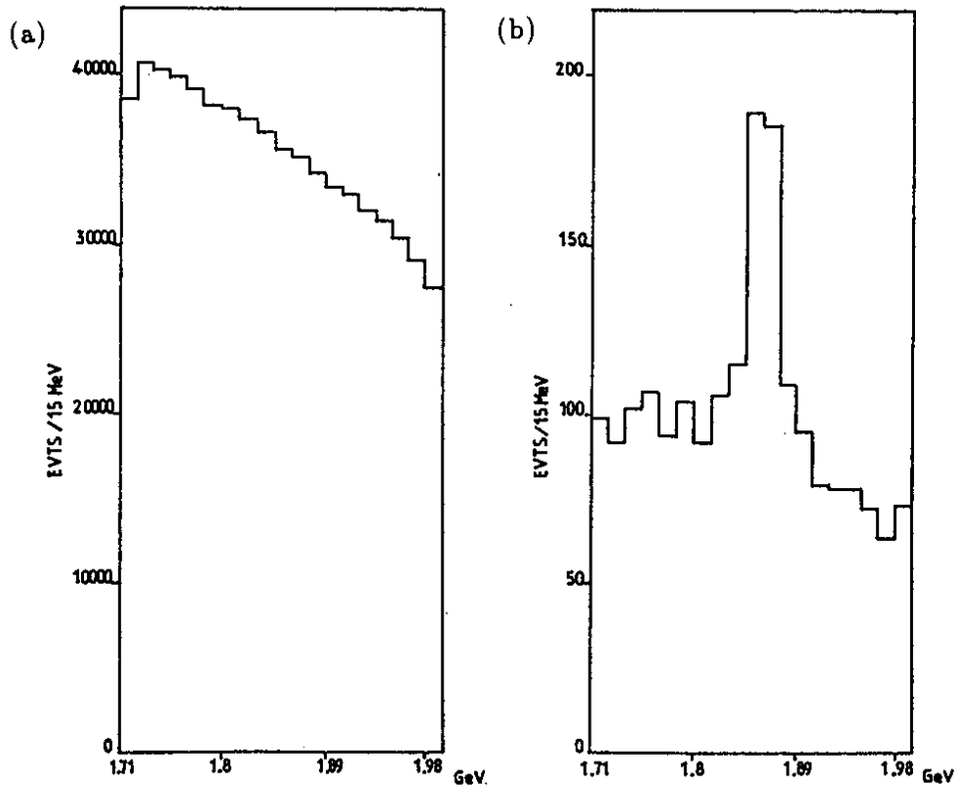

Fig. 3. $K^-\pi^+\pi^+$ mass distributions from data processed through the 3081 emulators:
(a) with no cut on the separation of primary and secondary vertices;
(b) with an $N_\sigma > 6$ cut on the vertex separation.

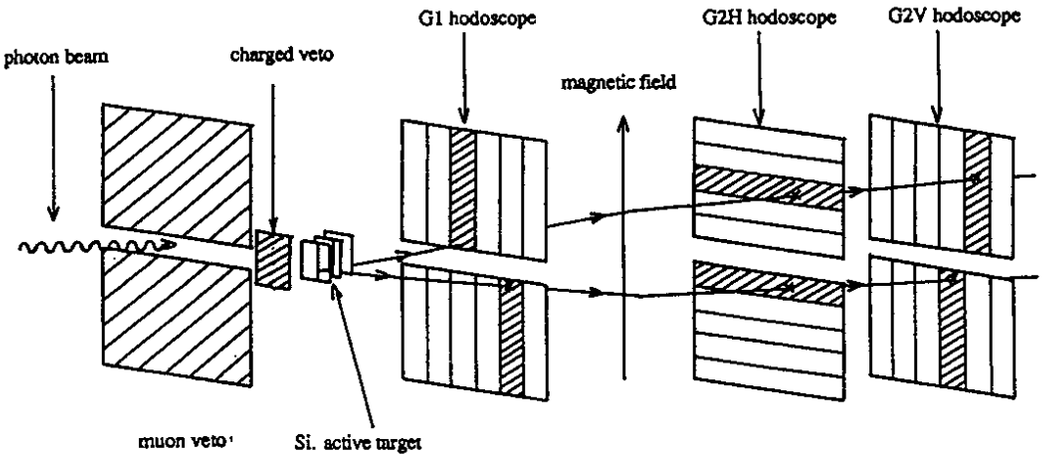

Fig. 4. Trigger conditions.

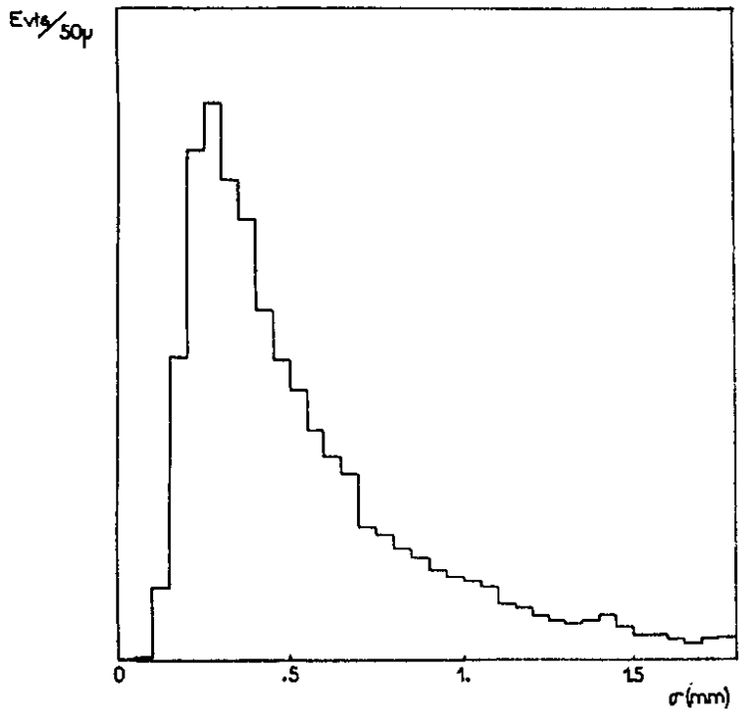

Fig. 5. Longitudinal accuracy of the $K\pi$ vertex.

(a)

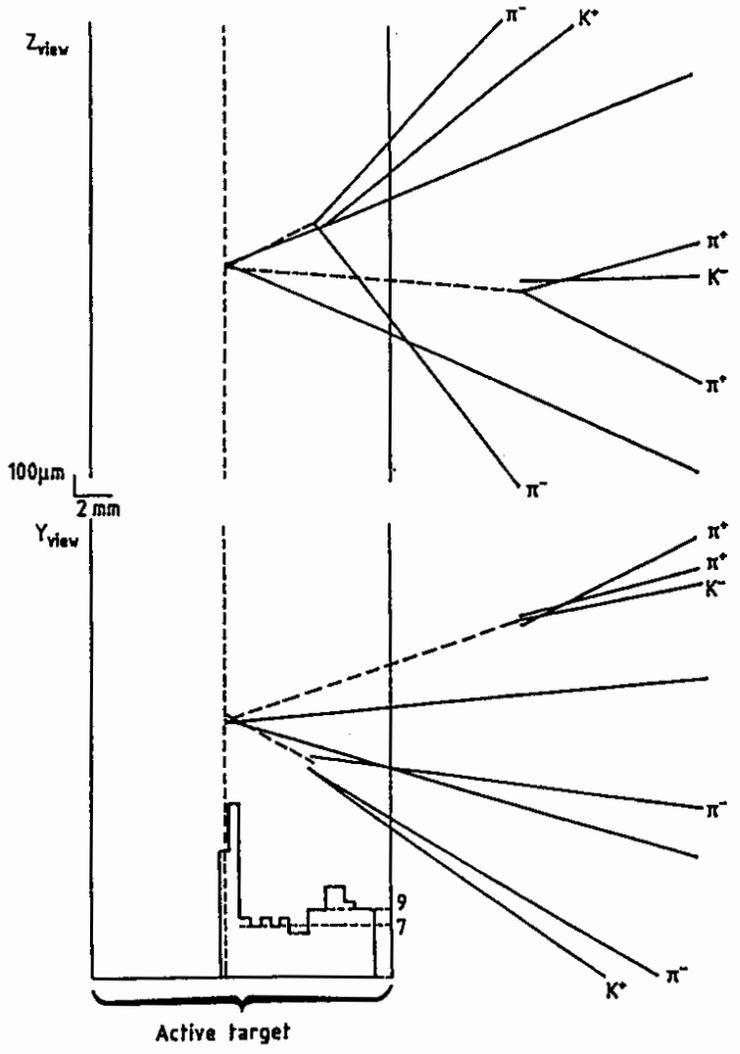

(b)

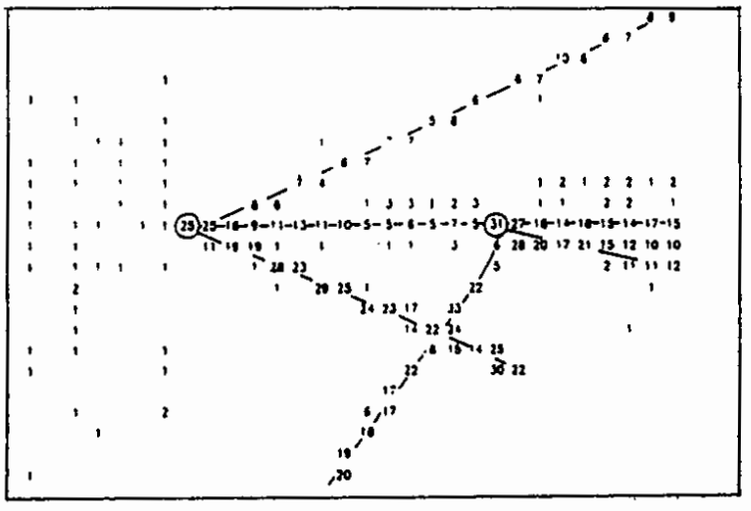

Fig. 6. (a) An event with both charmed particles reconstructed;
(b) A secondary interaction.

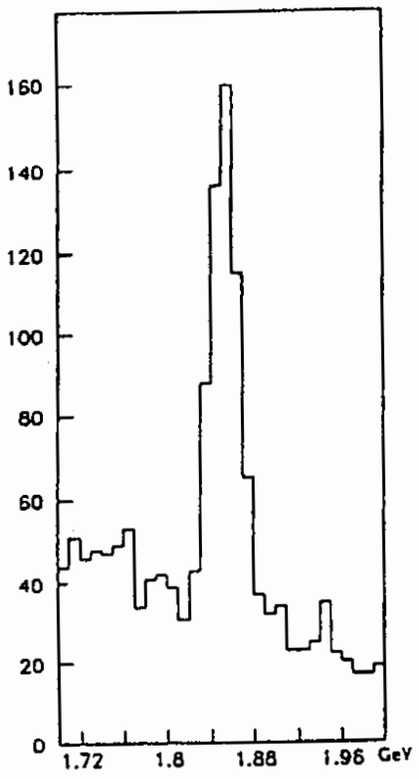

(a) $D^0 \to K^-\pi^+$ ($N_\sigma > 4$);

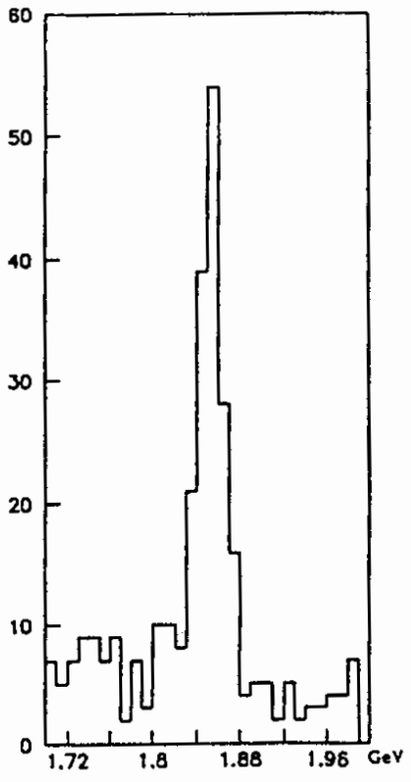

(b) $D^0 \to K^-\pi^+$ from D^{*+} ($N_\sigma > 1{\cdot}5$);

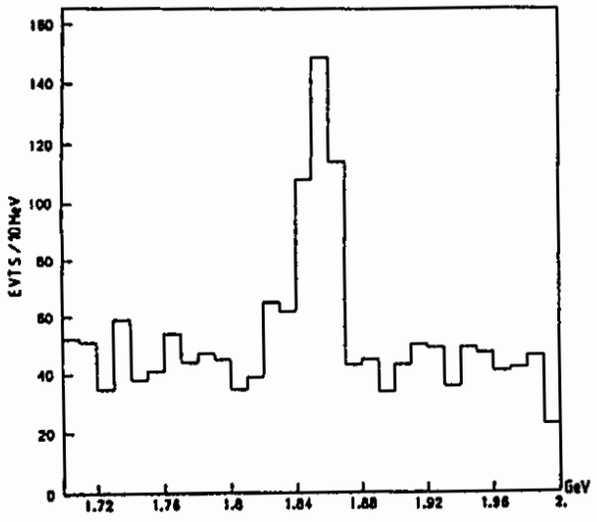

(c) $D^0 \to K^-\pi^+\pi^+\pi^-$ ($N_\sigma > 6$);

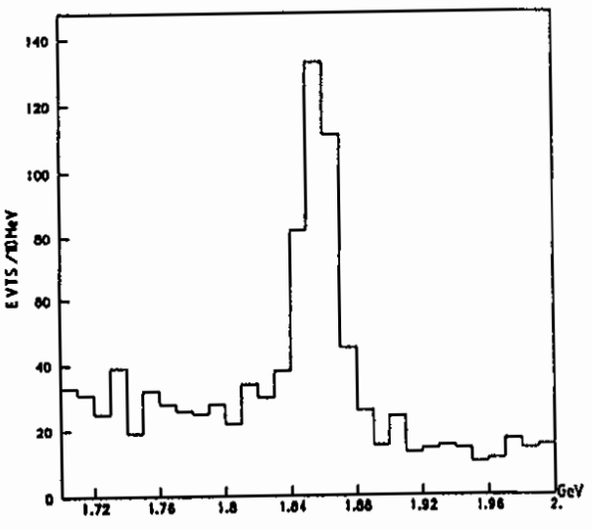

(d) $D^+ \to K^-\pi^+\pi^+$ ($N_\sigma > 4$).

Fig. 7. Inclusive D signals.

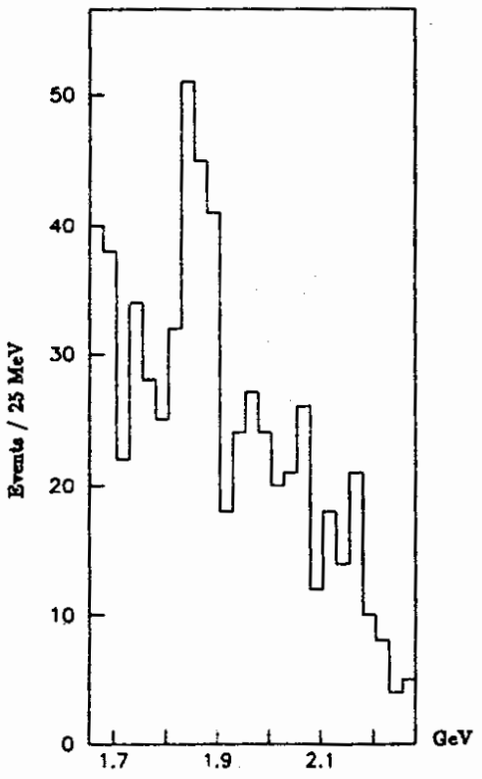

Fig. 8. $D^0 \to K^-\pi^+\pi^0$ mass distribution ($N_\sigma > 8$).

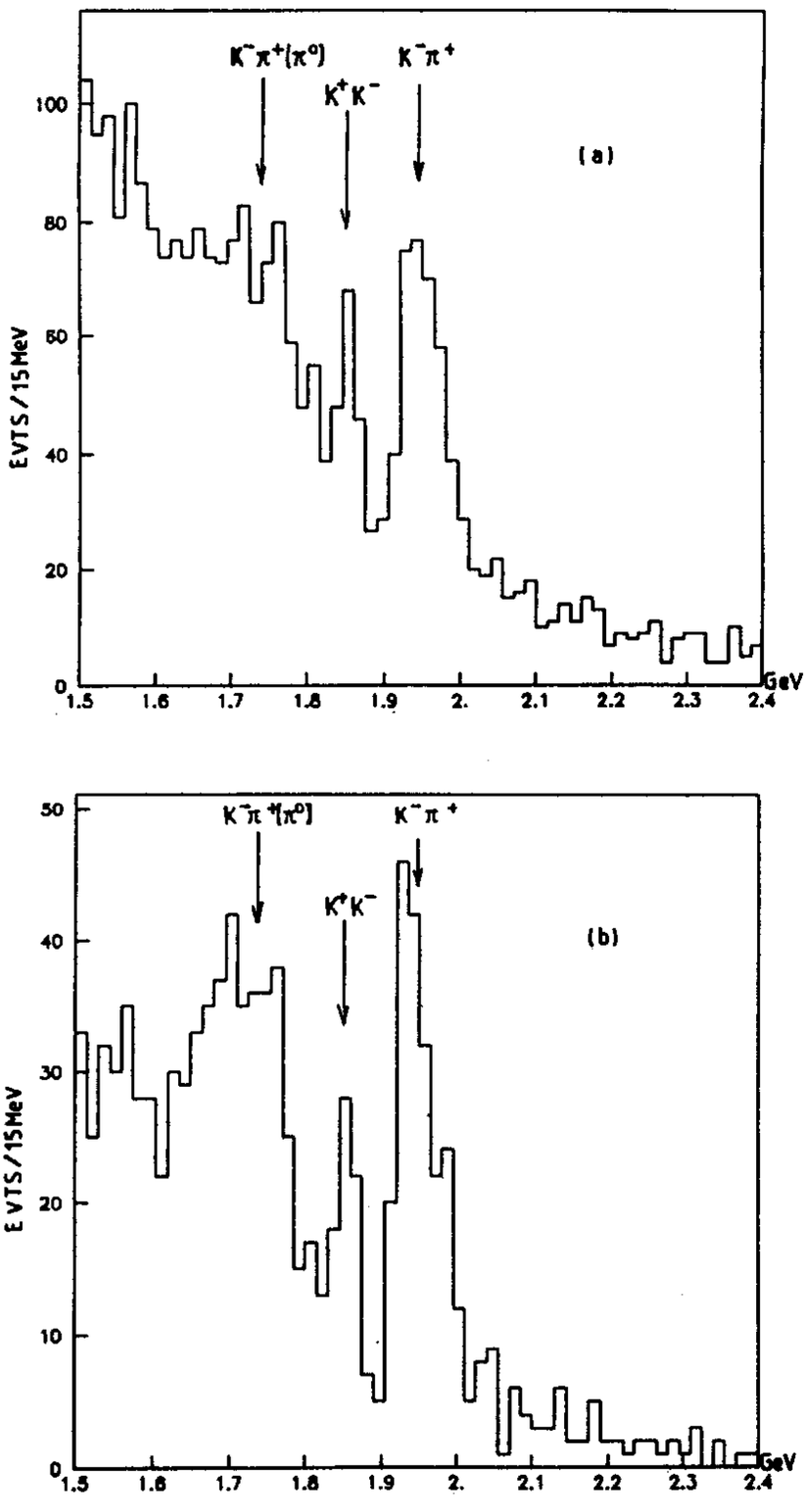

Fig. 9. $D^0 \to K^- K^+$ mass distribution:
(a) with an $N_\sigma > 2$ cut on the vertex separation.
(b) with an $N_\sigma > 5$ cut on the vertex separation.

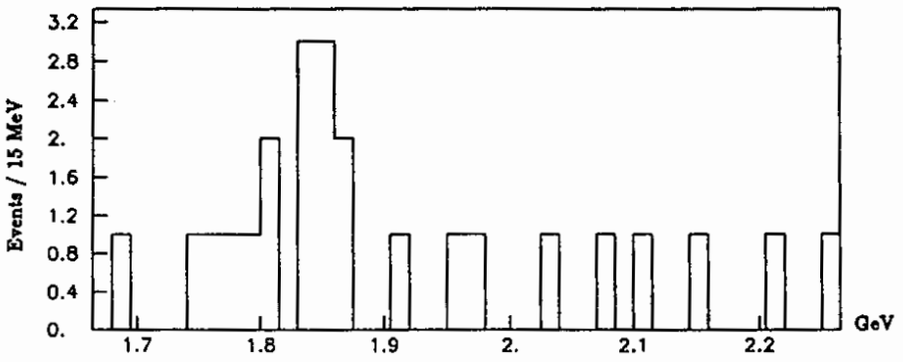

Fig. 10. $D^0 \to \phi\pi^+\pi^-$ mass distribution ($N_\sigma > 6$).

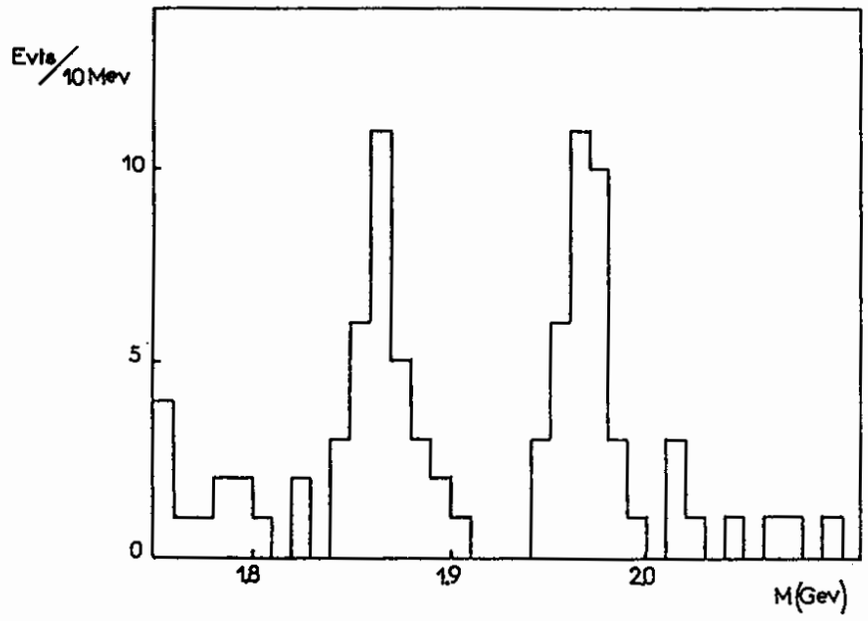

Fig. 11. $\phi\pi^+$ mass distribution ($N_\sigma > 2{\cdot}5$).

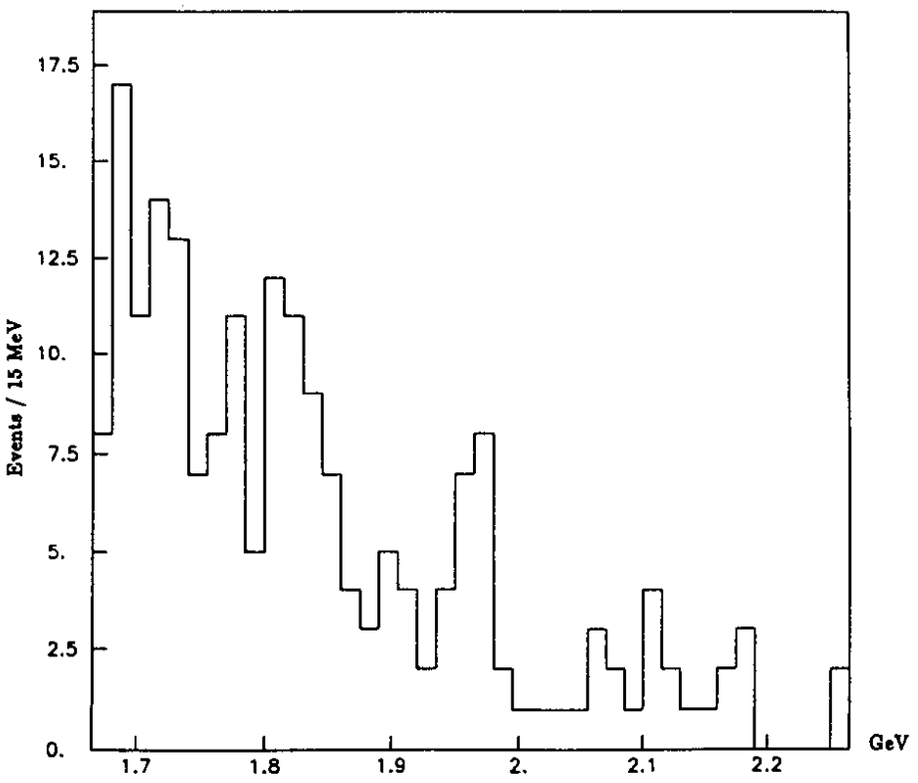

Fig. 12. $K^{*0}K^{+}$ mass distribution ($N_\sigma > 2$, identified kaons).

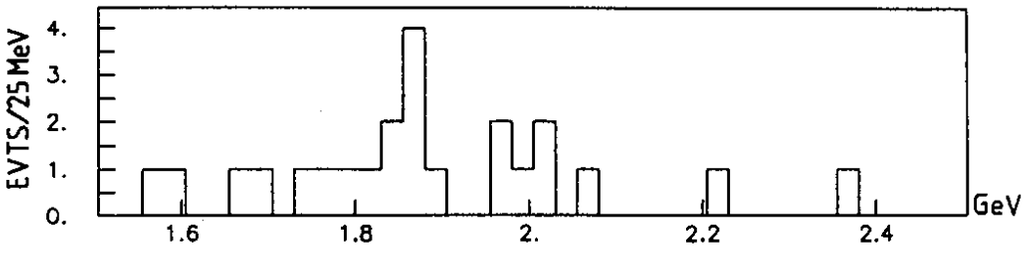

Fig. 13. $\phi\pi^{+}\pi^{0}$ mass distribution ($N_\sigma > 6$).

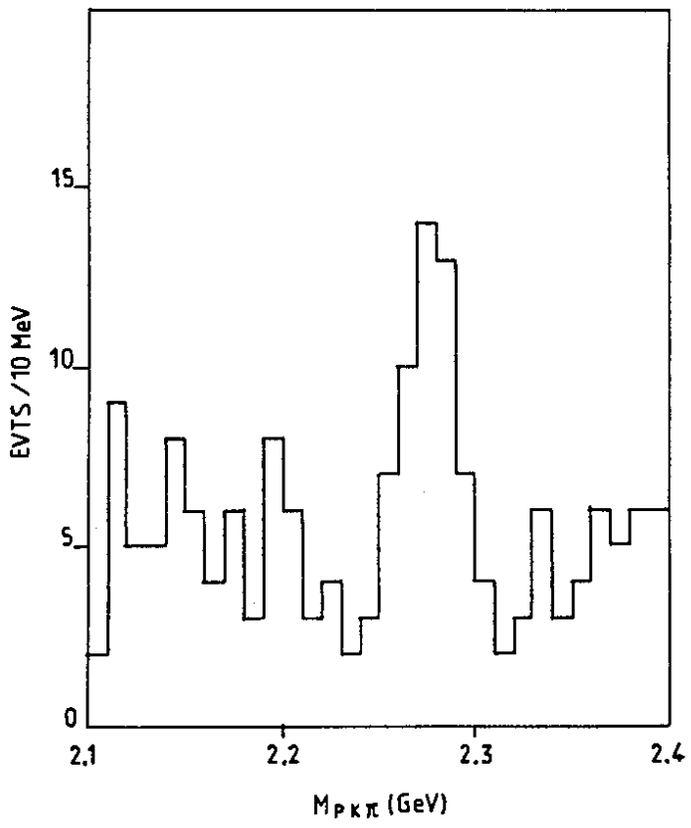

Fig. 14. $\Lambda_c \to pK^-\pi^+$ mass distribution ($N_\sigma > 3{\cdot}5$).

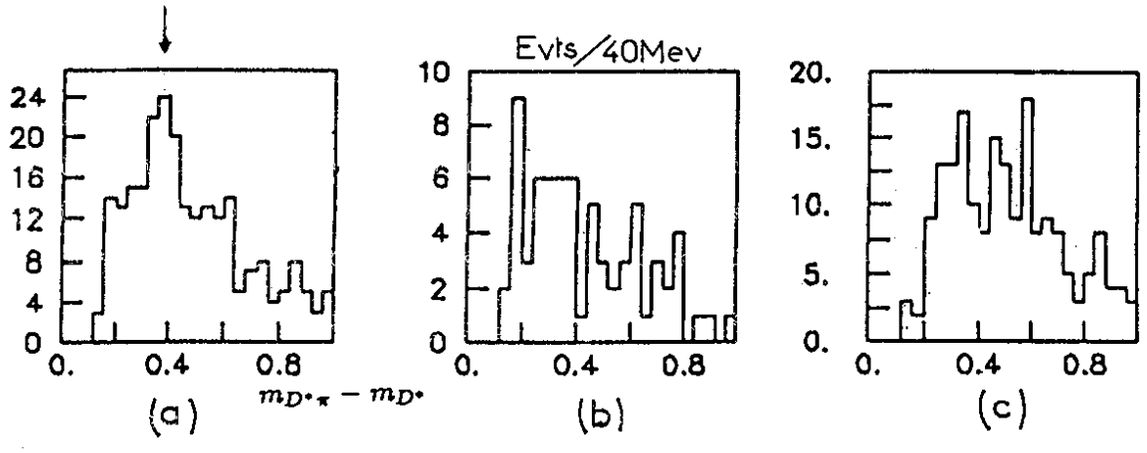

Fig. 15. Search for D^{**0}.

(a) Events in the D^{*+} mass region are used.

(b) Events in the wings of the D^{*+} signal are used.

(c) Wrong sign combinations.

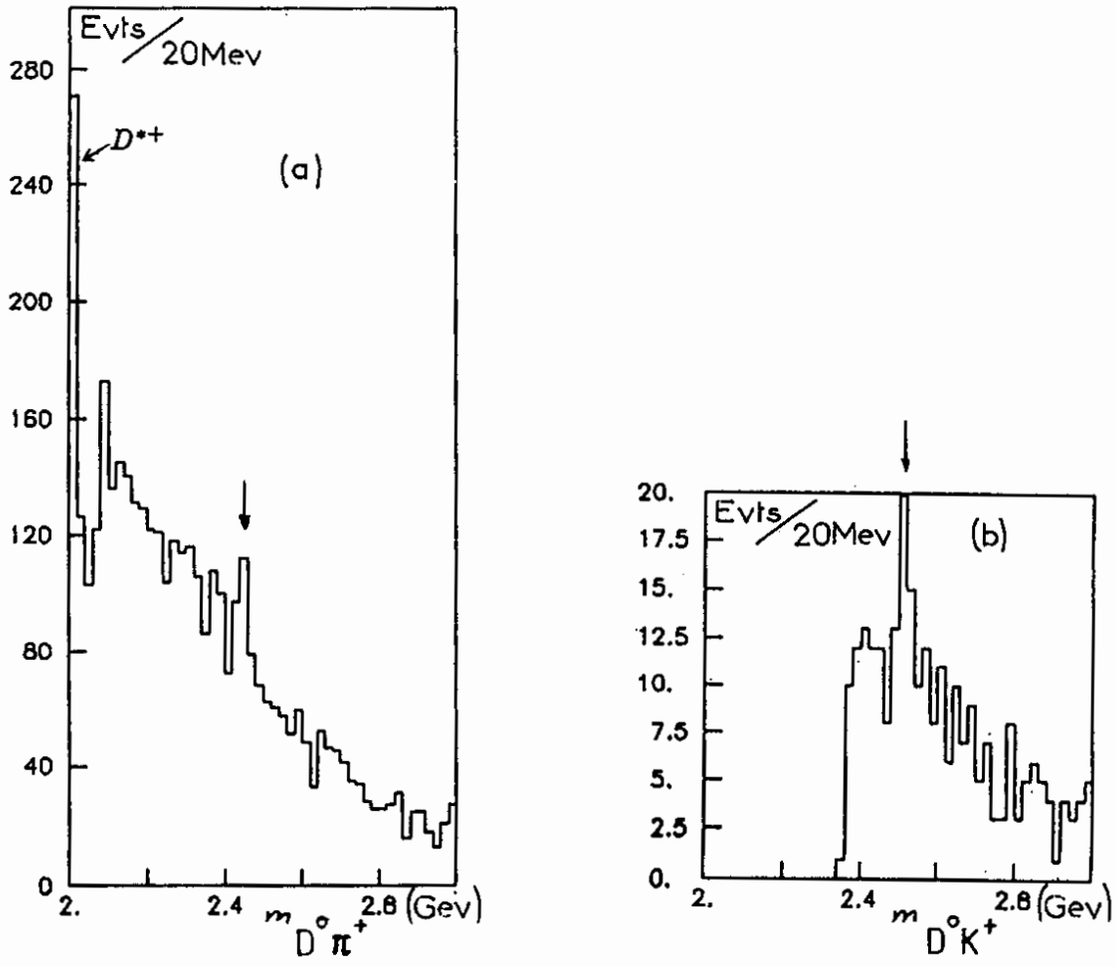

Fig. 16. (a) Search for D^{**+}, (b) Search for D_s^{**+}.

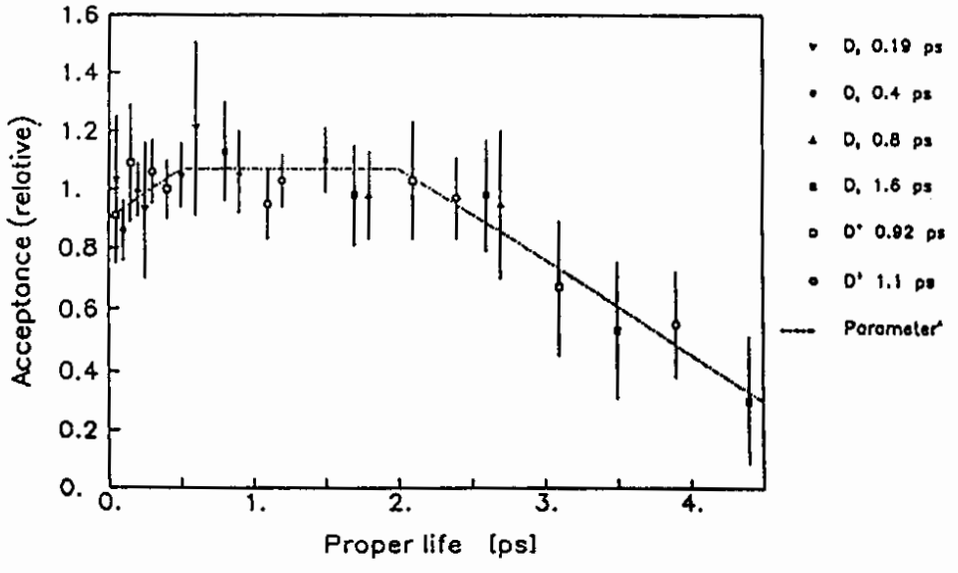

Fig. 17. Proper life acceptance for D_s lifetime.

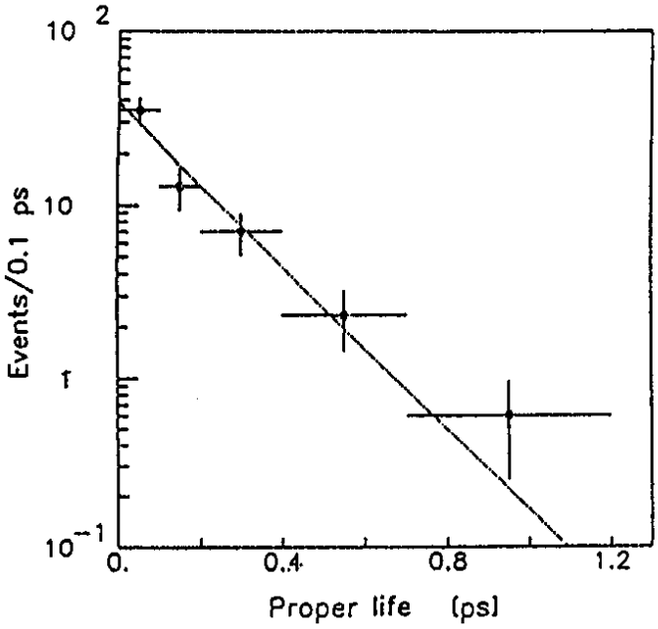

Fig. 18. Background proper life distribution for D_s analysis.

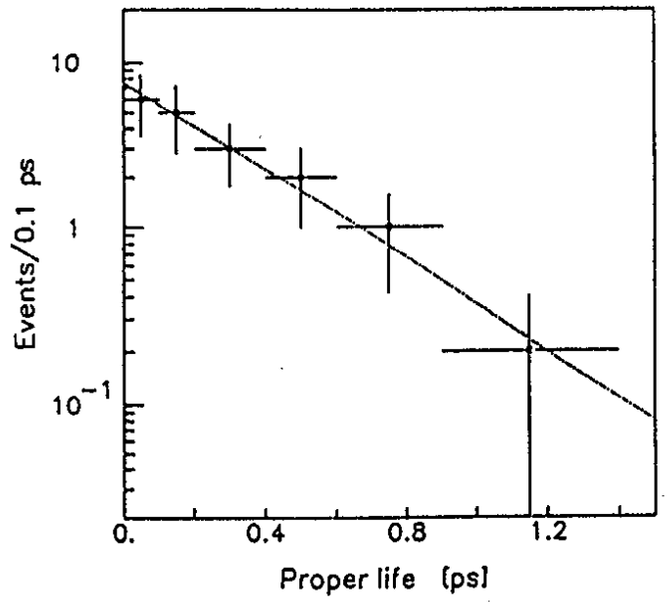

Fig. 19. D_s proper life distribution.

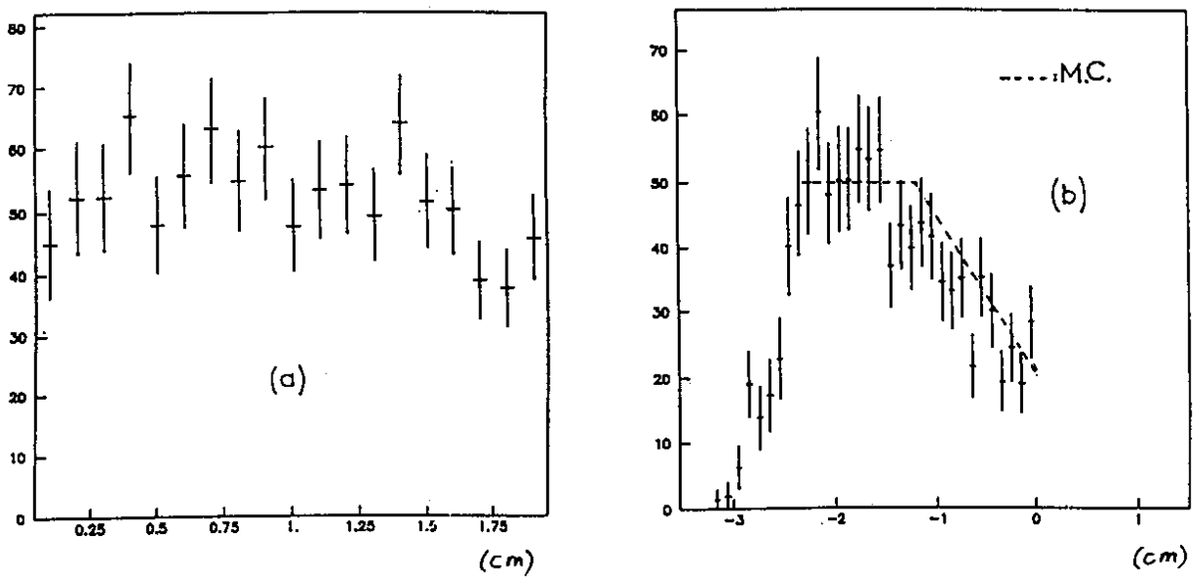

Fig. 20. Decay length acceptance for D^0.
(a) Number of reconstructed K_s^0 versus the distance between the K_s^0 decay vertex and the minimum decay distance (data are corrected for K_s^0 lifetime).
(b) Number of reconstructed K_s^0 versus the distance between the K_s^0 decay vertex and the first microstrip plane.

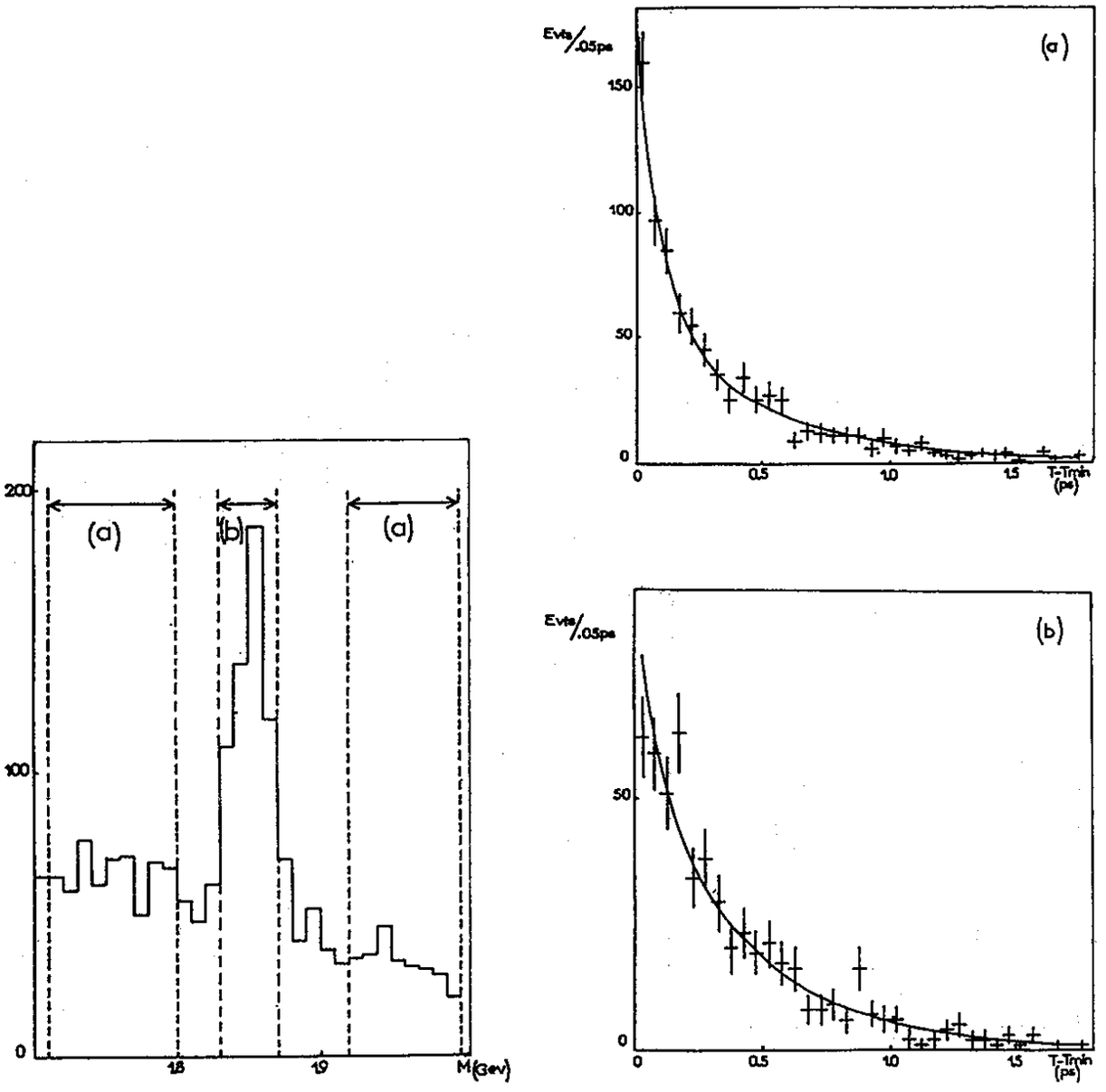

Fig. 21. (a) Background proper life distribution for D^0 analysis.
(b) D^0 proper life distribution.

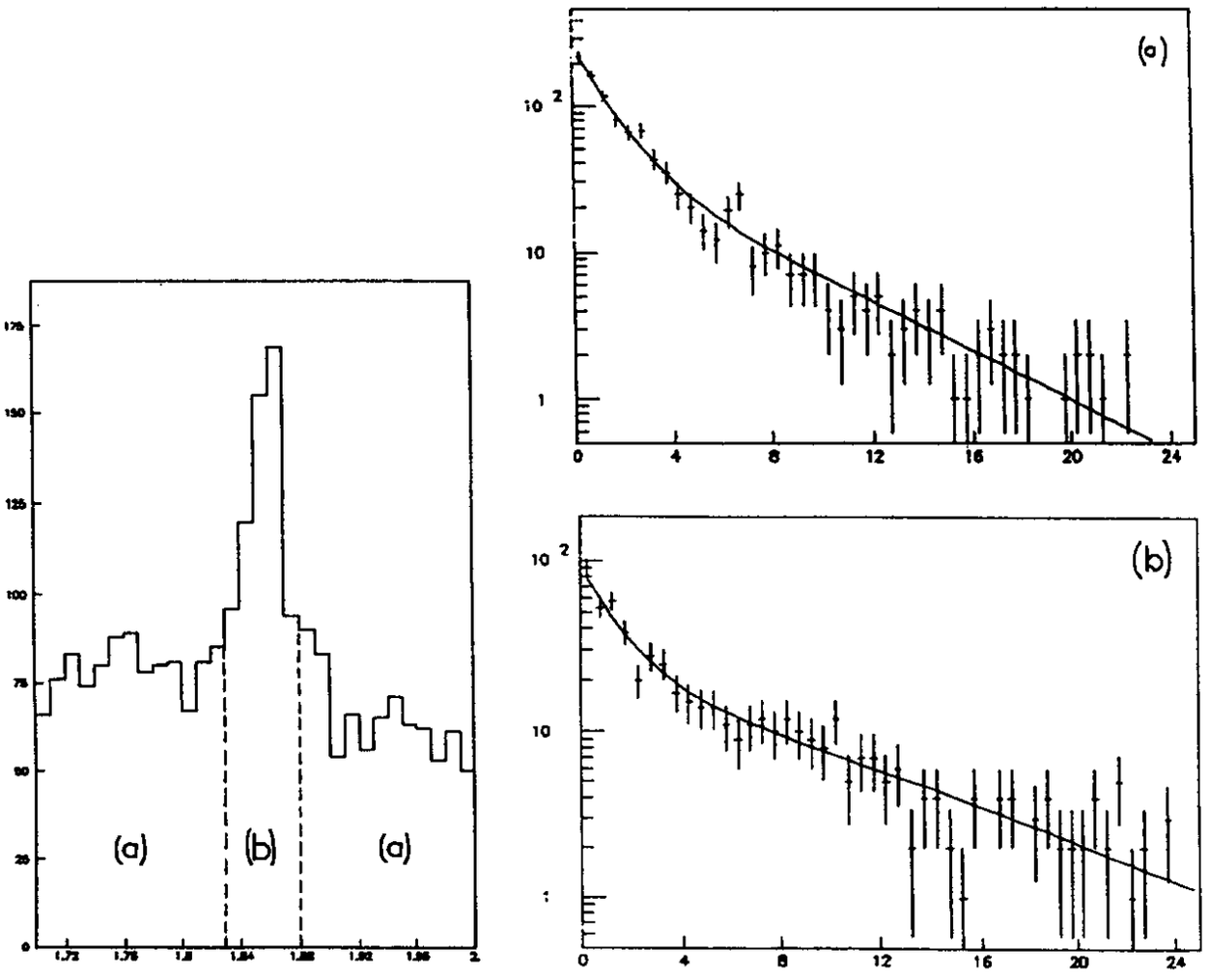

Fig. 22. (a) Background proper life distribution for D^+ analysis.
(b) D^+ proper life distribution.

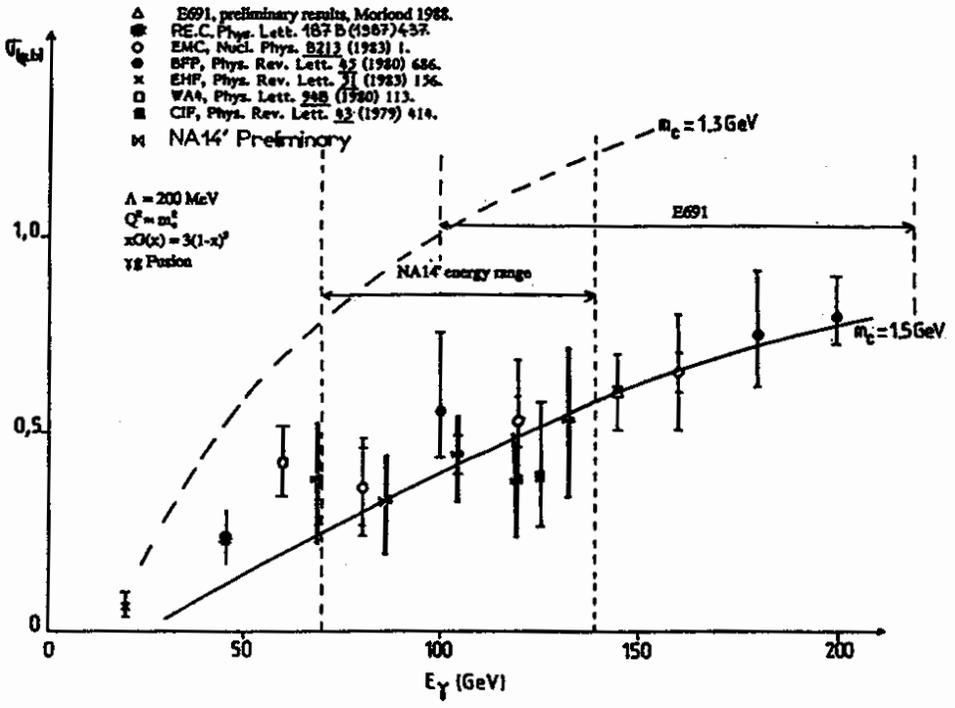

Fig. 23. Energy dependence of the charm photoproduction cross-section.

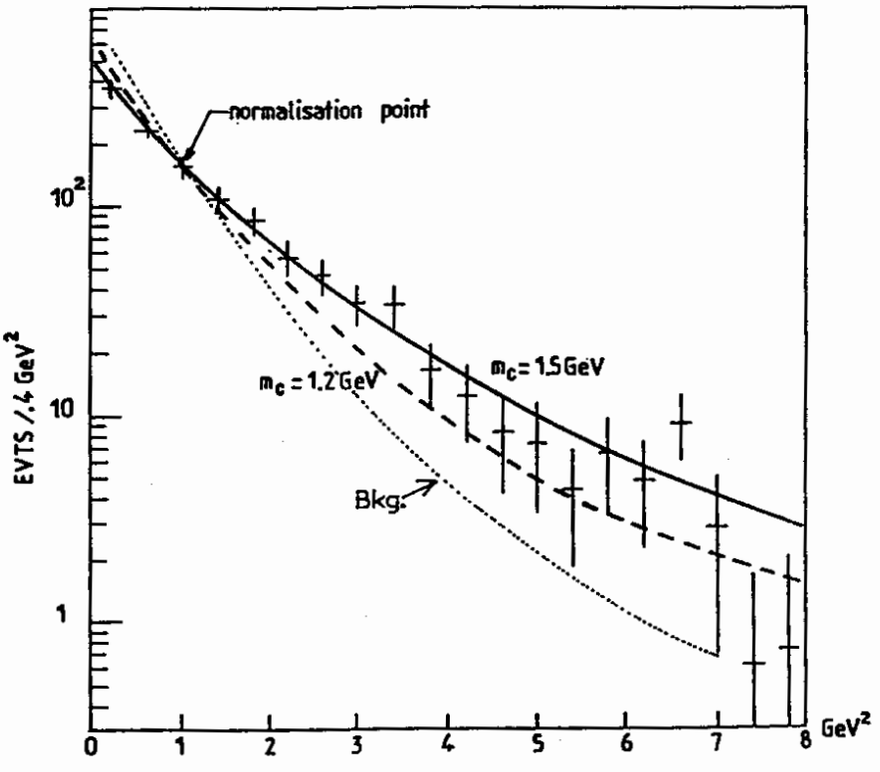

Fig. 24. p_T^2 distribution of D-mesons.

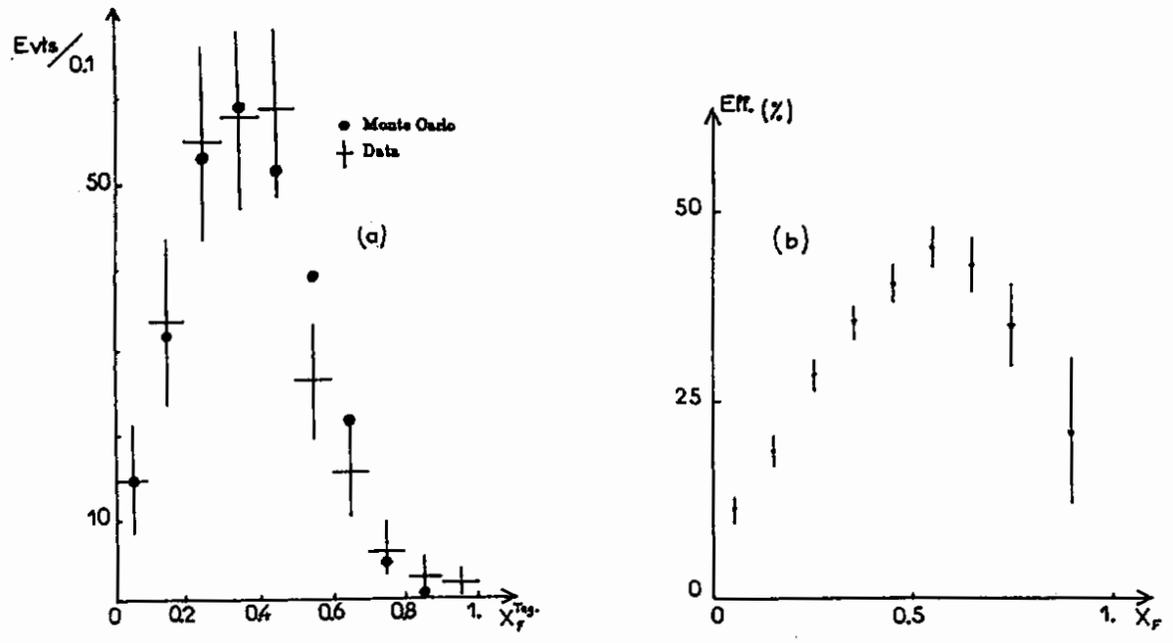

Fig. 25. (a) Measured x_F^{Tag} distribution of D^0-mesons.
The x_F^{Tag} quantity is computed using the total energy radiating by the incoming electron ($x_F^{Tag} \leq x_F$).
(b) Variation of the acceptance versus x_F

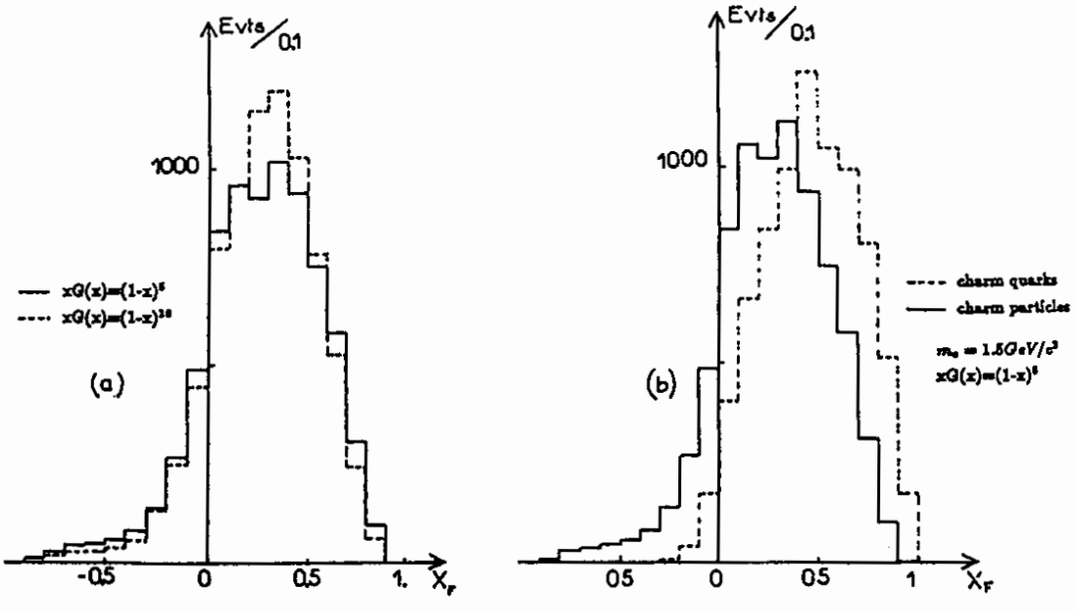

Fig. 26. (a) Expected x_F distributions for two choices of the gluon structure function. (detection efficiency not included)
(b) x_F distributions for charm quarks and for D mesons.

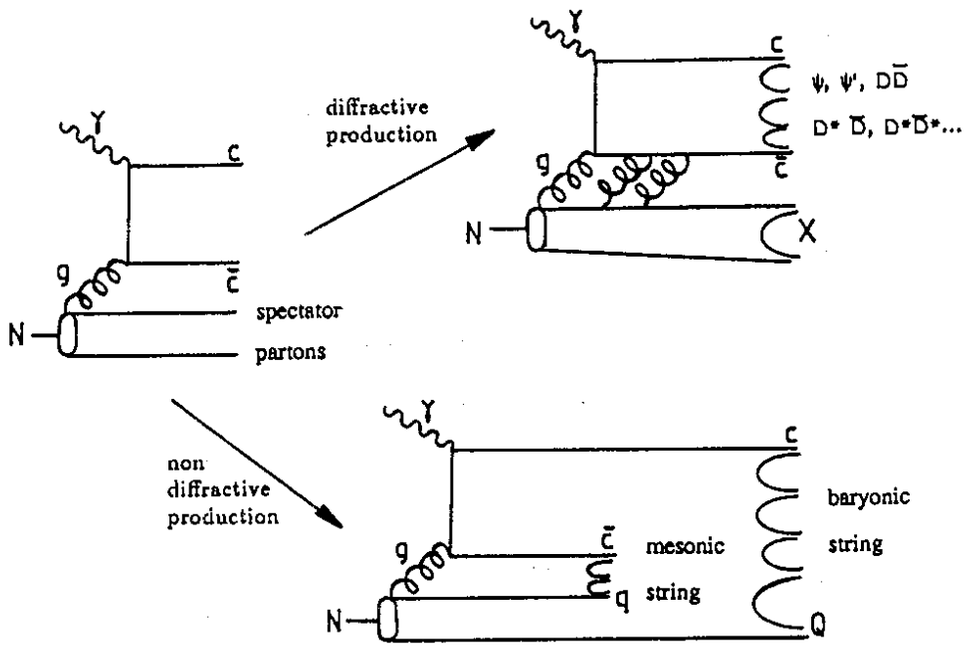

Fig. 27. Hadronisation schemes.

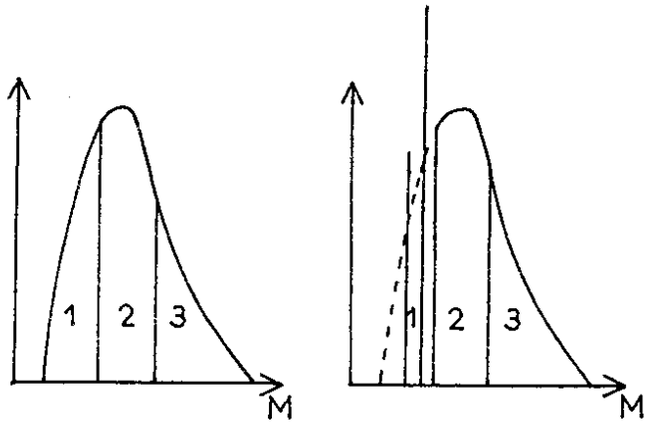

Fig. 28. Mass intervals used in the hadronisation scheme.

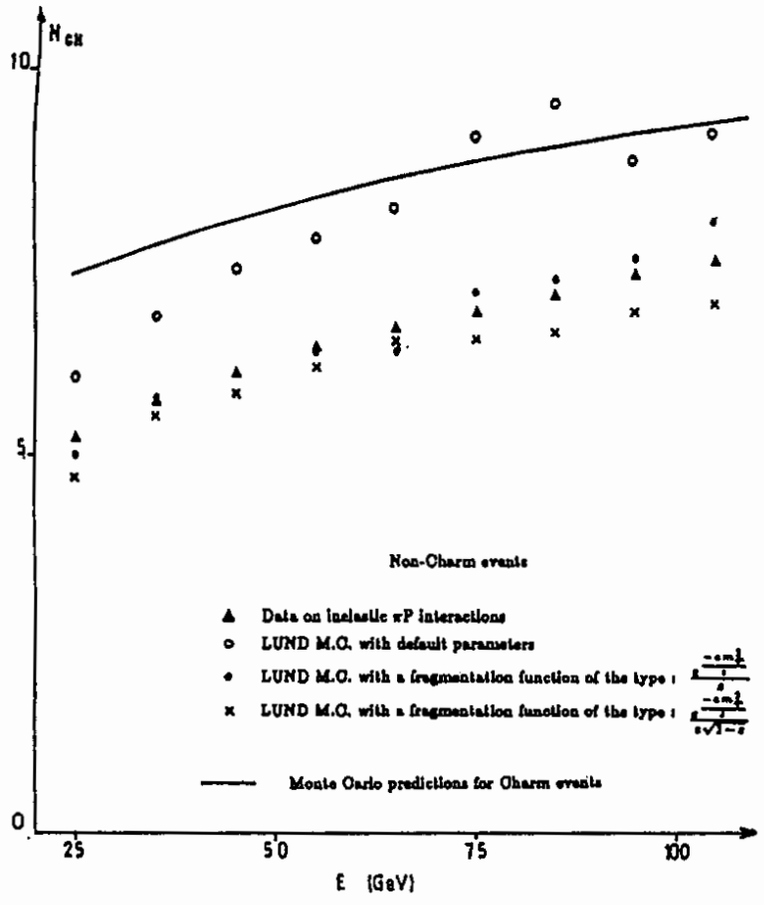

Fig. 29. Charged track multiplicity for non-diffractive events.

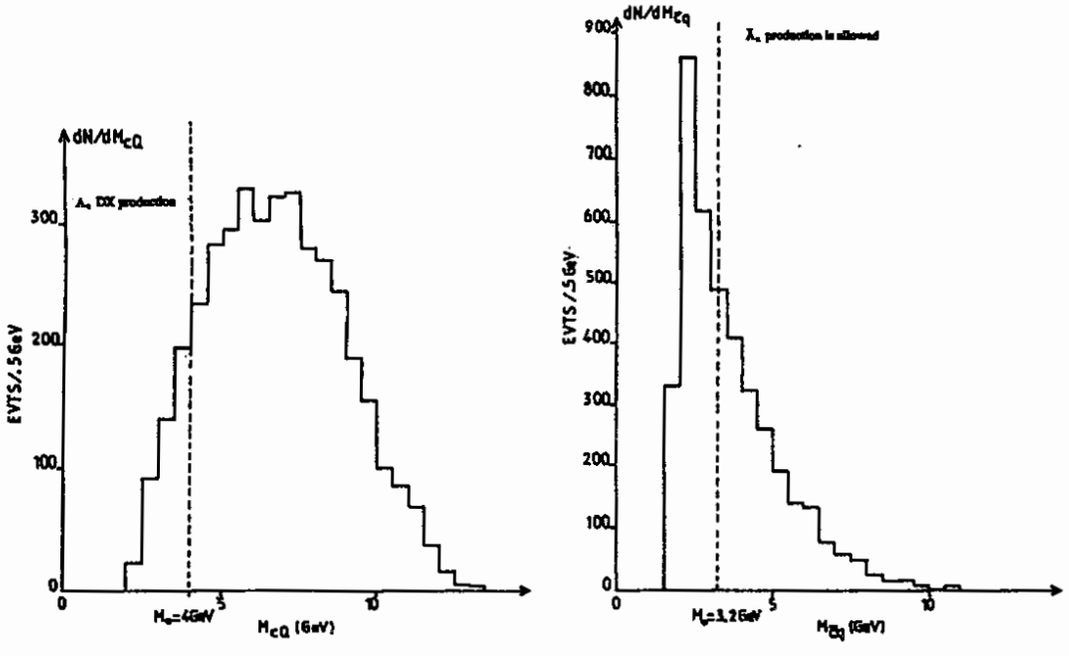

Fig. 30. String masses from the Dual Parton Model.

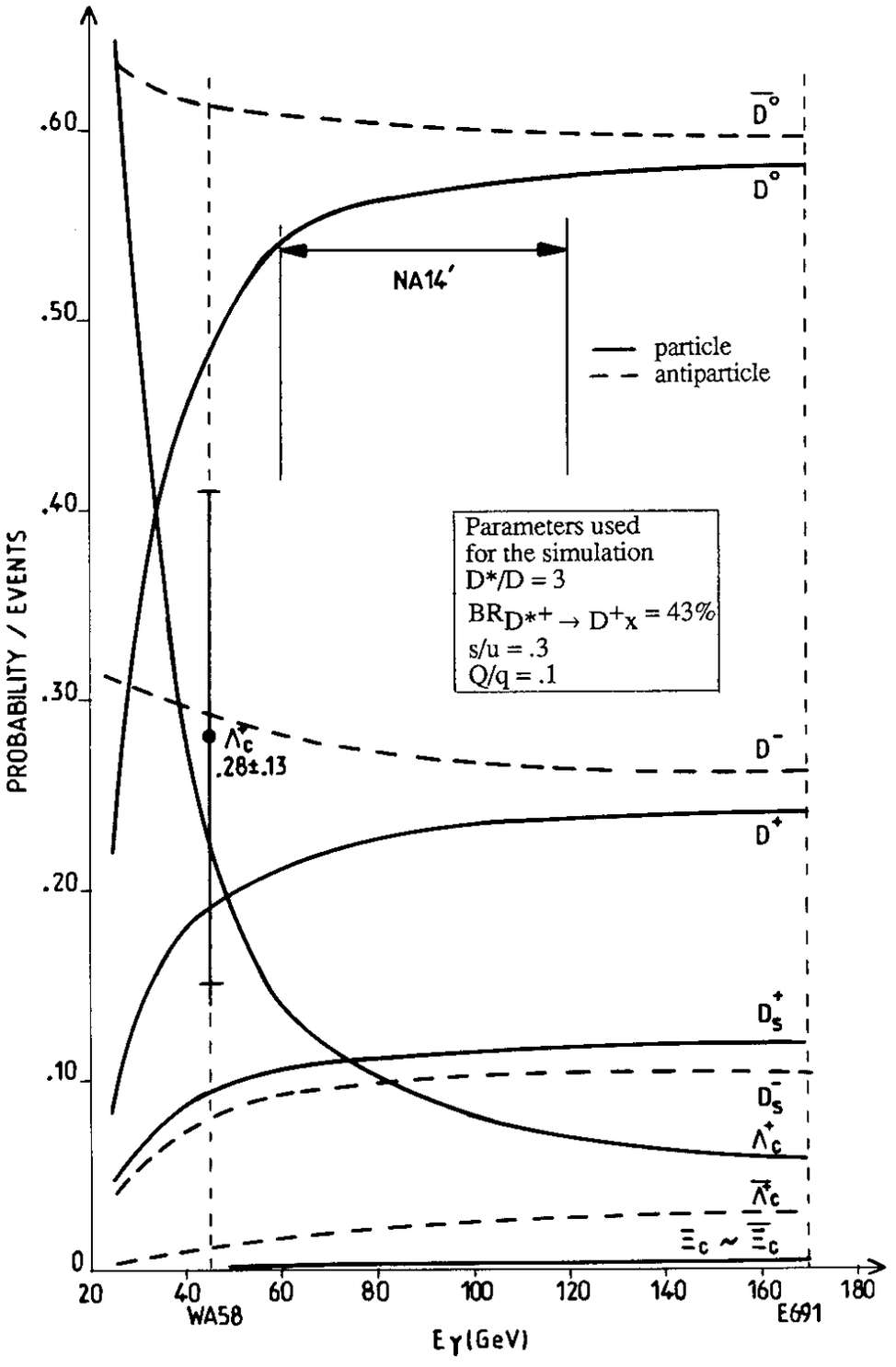

Fig. 31. Production rate predictions for charmed particles.